

CHALMERS UNIVERSITY OF TECHNOLOGY

DOCTORAL THESIS

---

**Nonlinear Electromechanics of  
nanomembranes and nanotubes**

---

Daniel Midtvedt

*A thesis submitted in fulfilment of the requirements  
for the degree of Doctor of Philosophy*

*in the*

Condensed Matter Theory group  
Department of Applied Physics

October 2013

Nonlinear Electromechanics of nanomembranes and nanotubes

DANIEL MIDTVEDT

ISBN 978-91-7385-922-6

© DANIEL MIDTVEDT, 2013.

Doktorsavhandlingar vid Chalmers tekniska högskola

Ny serie nr 3603

ISSN 0346-718X

Department of Applied Physics  
Chalmers University of Technology  
SE-412 96 Gothenburg  
Sweden  
Telephone + 46 (0)31-772 1000

Cover:

[en förklarande bildtext till eventuell omslagsbild,  
med sidhänvisning till utförligare information i uppsatsen.]

Chalmers Reproservice  
Gothenburg, Sweden 2013

# List of Included Papers

This thesis is based on the following papers, which are referred to in the text by their Roman numerals. The papers are not presented in chronological order.

I *Frequency tuning, nonlinearities and mode coupling in circular graphene resonators*

A. M. Eriksson, **D. Midtvedt**, A. Croy, A. Isacsson  
Nanotechnology, Vol. 24 (2013)

II *Nonlinear damping in graphene resonators*

A. Croy, **D. Midtvedt**, A. Isacsson, J. Kinaret  
Physical Review B, Vol. 86 (2012)

III *Intrinsic mode-coupling and thermalization in nanomechanical graphene drums*

**D. Midtvedt**, Z. Qi, A. Croy, H. S. Park, A. Isacsson  
arxiv:1309.1622 (2013) (*submitted to Physical Review Letters*)

IV *Determination of the Bending Rigidity of Graphene via Electrostatic Actuation of Buckled Membranes*

N. Lindahl, **D. Midtvedt**, J. Svensson, O. A. Nerushev, N. Lindvall, A. Isacsson,  
E. E. B. Campbell  
Nano Letters, Vol. 12 (2012)

V *Parametric Resonance in Nanoelectromechanical Single Electron Transistors*

**D. Midtvedt**, Y. Tarakanov, J. Kinaret  
Nano Letters, Vol. 11 (2011)

Not included in the thesis is the following publication.

- *Carbon Nanotube Field Effect Transistors with Suspended Graphene Gates*  
J. Svensson, N. Lindahl, H. Yun, M. Seo, **D. Midtvedt**, Y. Tarakanov, N. Lindvall, O. A. Nerushev, J. Kinaret, S. W. Lee, E. E. B. Campbell  
Nano Letters, Vol. 11 (2011)

# *Abstract*

Department of Applied Physics

Doctor of Philosophy

## **Nonlinear Electromechanics of nanomembranes and nanotubes**

Daniel Midtvedt

Nanomechanical resonators is a class of systems consisting of resonating structures on the sub-micrometer scale. They are known to display strong nonlinear dynamics. In addition, due to the size of the systems ( $\sim 10^4 - 10^6$  atoms), a statistical description of the internal degrees of freedom is not a priori justified, and they are typically critically affected by fluctuations. This hampers the straightforward miniaturization of currently employed micromechanical systems, but it also introduces new and interesting physics. In particular, an improved description and understanding of the nonlinear effects in these systems will enable the exploitation of these effects.

In this thesis, a theoretical framework for describing the elastic properties of low-dimensional resonators, such as suspended graphene and nanotube structures, is developed. The framework is based on continuum mechanics, which is the same underlying model that describes the properties of macroscopic rods and plates. However, the reduced dimensionality of the considered system introduces some interesting aspects of the theory. The nonlinearities are characterized in Paper I and Paper II and exploited in the subsequent papers:

- To gain additional insight to the process of relaxation and thermalization in mesoscopic systems (Paper III);
- To develop a method for experimentally determining the bending rigidity of atomically thin membranes (Paper IV) and
- To study the interplay between mechanical motion and single electron tunneling in suspended carbon nanotubes (Paper V).

Due to the theoretical nature of the thesis, special attention is given to the possibility of experimental observation of the physical effects presented.

# *Acknowledgements*

Writing this thesis has given me the pleasurable opportunity to reminisce and acknowledge the support of family, friends and colleagues.

First of all, I would like to thank Jari Kinaret for introducing me to the Condensed Matter Theory group almost four years ago, and for your continuing support.

Andreas and Alex, your office doors have always been open and your ears always susceptible to my stupid thoughts and ideas.

Thanks are also due to all my colleagues in the CMT group, for providing such a fun and inspiring working environment.

However, the completion of this academic work has relied also on non-academic stimulation: without the commitment of my dearest friends, my fate would have been and will invariably be to languish in the shady solitude of my office. Although naming all people that have prevented this fate is an impossible task, I would like to thank Henrik and Karl for literally dragging me out of my office. Our regular discussions on relaxation times in fusion plasmas, exercise and life in general have been highlights in my everyday routine.

Last but not least, my lovely Ingrid, for your invaluable support both in times of despair and of joy. Thanks you you, the agonizing process of writing this thesis has been the happiest period of my life.

# Contents

<b>Abstract</b>	<b>iii</b>
<b>Acknowledgements</b>	<b>iv</b>
<b>Contents</b>	<b>v</b>
<b>List of Figures</b>	<b>vii</b>
<b>1 Introduction</b>	<b>1</b>
1.1 Hamiltonian dynamics . . . . .	3
1.2 Statistical mechanics . . . . .	6
1.3 Carbon based nanomaterials . . . . .	8
1.3.1 Carbon and NanoElectroMechanical Systems (NEMS) . . . . .	11
<b>2 Continuum mechanical description of nanoresonators</b>	<b>12</b>
2.1 Equation of motion for a nanodrum . . . . .	15
2.1.1 Equations of motion for carbon nanotubes; effect of bending . . . . .	16
2.2 Actuated nanoresonators . . . . .	17
<b>3 Dissipation and relaxation in graphene resonators</b>	<b>20</b>
3.1 FPU problem . . . . .	22
3.2 Dissipation in graphene resonators coupled to a medium . . . . .	24
3.3 Thermalization of nanoscale resonators . . . . .	29
3.4 Internal relaxation in nanobeams . . . . .	31
3.5 Drum geometry . . . . .	32
<b>4 Bending rigidity of graphene</b>	<b>38</b>
4.1 Bending rigidity of graphene: current status . . . . .	38
4.2 Measuring the bending rigidity . . . . .	40
<b>5 Parametric excitation of carbon nanotube single electron transistors</b>	<b>44</b>
<b>6 Summary</b>	<b>50</b>
<b>A Equation of motion for nanobeam</b>	<b>52</b>
A.1 Response of nanobeam to static force . . . . .	54

---

A.2 Dynamical response of nanobeam . . . . .	54
<b>B Equation of motion for graphene sheet coupled to elastic substrate</b>	<b>57</b>
<b>C Scaling of snap-through voltage for drum and beam structures</b>	<b>61</b>
<b>Bibliography</b>	<b>68</b>

# List of Figures

1.1	Schematic image of a graphene sheet, showing the carbon atoms arranged in a hexagonal lattice. . . . .	9
1.2	An archetypal graphene NEMS structure. A graphene sheet is suspended over a trench in the substrate. Mechanical motion of the graphene is induced by applying a voltage to the gate below it. The size of the structure is typically in the range 10 nm - 10 $\mu\text{m}$ . . . . .	11
2.1	The geometries considered in this thesis. a) Beam geometry, b) Drum geometry. . . . .	14
2.2	The renormalized resonance frequency as a function of gate voltage for a drum (dashed line) and beam (full line) with parameters as given in the main text. The drum displays less mechanical stiffening compared to the beam. . . . .	19
3.1	The scaling of the imaginary part of the overlap integrals for beams (squares) and drums (circles) with frequency in logarithmic scale. The dashed lines correspond to least square fits proportional to $\Omega^3$ for the beams and $\Omega$ for the drums . . . . .	27
3.2	The quality factor $Q$ as a function of bias voltage $V_{\text{dc}}$ . The quality factor is evaluated for $V_{\text{ac}} = 10 \mu\text{V}$ (blue line), $V_{\text{ac}} = 100 \mu\text{V}$ (black line) and $V_{\text{ac}} = 1 \text{ mV}$ (green line). . . . .	28
3.3	Time evolution of the modal energies evaluated from the continuum theory, when initially all energies in the 16th mode. Mode numbers are indicated on the right. The higher modes equilibrate quickly, while the lowest modes are essentially decoupled from the dynamics. . . . .	34
3.4	a: Simulation of mode coupled equations for a fixed total energy, but with varying initial energy in fundamental mode. By shifting time, the curves align. The solid line is a fitted sigmoid function used to extract the transition time $\tau_{tr}$ . b: Extracted rates $\Gamma = \tau_{tr}^{-1}$ from MD simulations (filled symbols) and continuum mechanics (open symbols). The dashed line corresponds to a linear scaling with dimensionless energy. . . . .	36
3.5	Fundamental mode frequency as a function of mode energy. Symbols correspond to molecular dynamics results, while the full line is the curve predicted from continuum mechanics. . . . .	37
4.1	Visualisation of the buckled structures. The upper image is a schematic image of the resulting structure. Beneath it to the left is an AFM image of an experimental structure, and to the right an STM image. In both images the resulting curvature is clearly visible. . . . .	39

4.2	A doubly clamped structure showing a snap through instability. a) and b) are AFM images of the sample at 0 V and 3 V, respectively. In c), AFM sweeps have been made along the dashed line in a) while gradually increasing the voltage. In d) the AFM tip is kept fixed at the spot marked with a cross in a) while gradually increasing the voltage. Here, the snap-through instability manifests itself as the discontinuity in tip position at 2.6 V. . . . .	41
4.3	A fully clamped structure showing a snap through instability. a) and b) are AFM images of the sample at 0V and 3V, respectively. In c), AFM sweeps have been made along the dashed line in a) while gradually increasing the voltage. In d) the AFM tip is kept fixed at the spot marked with a cross in a) while gradually increasing the voltage. Here, the snap-through instability manifests itself as the discontinuity in tip position at 3V. . . . .	42
4.4	Scaling of the snap-through voltage with radius of curvature for fully clamped bilayer drums. The full line is a least squares fit, while the dashed lines represent the uncertainty. The scaling is consistent with theoretical considerations. . . . .	43
4.5	Scaling of the snap-through voltage with radius of curvature for doubly clamped beams. The open diamonds are monolayers, full diamonds bilayers and open square trilayer. The scaling is consistent with theoretical considerations. . . . .	43
5.1	Visualization of the considered structure. A carbon nanotube with a quantum dot residing on it is coupled via tunneling barriers to two electrodes, source and drain. Beneath the tube there is a gate electrode capable of shifting the chemical potential of the quantum dot. Image provided by Yury Tarakanov. . . . .	45
5.2	Energy diagram showing the concept of the single electron transistor. Tunneling is prohibited unless the chemical potential of the dot is aligned with the chemical potential of the leads. By biasing the transistor, tunneling in either direction can be enhanced. . . . .	46
5.3	The resonance shift due to single electron tunneling as a function of the misalignment in chemical potentials of dot and lead at various source-drain voltages. The shift is strongly peaked at the degeneracy point, where the chemical potentials align. The inset shows the frequency shift at the degeneracy point as a function of source drain voltage. Applying an oscillating source-drain voltage causes an oscillatory frequency shift. . . . .	48
5.4	Contour plot of the deflection amplitude (in nanometers) at the modulation frequency $\omega \approx \omega_1$ when the dot is biased at the degeneracy point. Note the boomerang shape of the region where the excitation occurs. The inset shows the time evolution of the oscillations inside and outside the region of parametric instability . . . . .	49
A.1	Maximal flexural deformation $w(0)$ as a function of the applied pressure $P_z$ . The dotted lines are the corresponding asymptotic scalings. . . . .	55

- 
- C.1 A schematic view of the process of snap through. Left: For small pressures a local deformation is formed in the region denoted  $\Omega$ . Middle: When the critical pressure is reached, it becomes energetically favorable to form a concave region where the elastic energy is confined to a narrow region  $\Gamma$ . Right: This concave region is elastically unstable. As a result, the deformation propagates outward, and the sheet snaps through. . . . . 62
- C.2 Top: Shells under external pressure display two qualitatively different regions of deformation, indicated in the figure by the dashed and dash-dotted line. At low pressures, the shell will locally flatten, decreasing the local curvature. For large pressures, the deformed part of the shell will form a mirror image of its undeformed counterpart. The main contribution to the elastic energy will then be contained in a narrow region close to the edge of the deformed region. Bottom: Close-up of the edge of the deformation for large pressures. The edge region can be parametrized by a width  $\delta$  and an angle  $\alpha$ . . . . . 62



# Chapter 1

## Introduction

Using a term like nonlinear science is like referring to the bulk of zoology as the study of non-elephant animals

---

Stanislaw Ulam

The world around us is inherently nonlinear. From a child sitting on a swing, to large scale fluctuations in the climate, a vast majority of the systems we encounter in our everyday lives display nonlinear dynamics. In fact, as will be discussed at great length in a subsequent chapter, the fundamental concepts of thermodynamics and statistical mechanics rely on nonlinearities. Still, throughout history, the field of physics has mainly dealt with linear systems.

The reason for this apparent inconsistency can be put quite simply: linear systems are solvable, while nonlinear systems in general are not. Therefore physicists often go to great lengths to reduce nonlinear systems to linear ones, hoping that the key physics is not lost in the process.

This approach gave reasonable results because physics, up until the 20th century, was concerned with the behavior of macroscopic objects: apples falling from trees, vibrating plates and swinging pendulums. It is clear that to solve for the motion of the swinging pendulum, one does not have to solve the equations of motion for each individual atom in the pendulum, but it is sufficient to look at the average motion of all atoms. So, even if, as is generally the case, the individual atoms behave in a complicated, nonlinear fashion, the macroscopic system can be described by a single equation of motion which in many cases may be approximated as linear. In mechanical systems there often exist a length scale that sets the regime of validity of such linearized equations. Correspondingly, vibrating plates behave linearly if their vibration amplitude is small compared to the thickness of

the plate, and a pendulum behaves linearly if the amplitude is small compared to the length of the pendulum.

At the turn of the 20th century, quantum mechanics made it possible to consider also the internal degrees of freedom. But although quantum mechanics revealed a whole new world of physics, still only linear, few degrees of freedom systems were tractable, such as the energy levels of a single hydrogen atom.

Simultaneously, thermodynamics and statistical physics had been developed as a tool to describe how physical systems interact with their environment, and how the statistical properties of the internal degrees of freedom affects the macroscopic properties. This introduced the concept of thermodynamic equilibrium as a state where no flow of energy occurs within the system. Considering small deviations from this hypothetical state, the equations for the internal degrees of freedom can be linearized and various macroscopical properties can be derived. However, this relies on a statistical description of the internal degrees of freedom, e.g. the motion of the individual atoms. This is possible if the number of atoms is very large and the time scale of interest is large compared to the natural time scales of the internal degrees of freedom.

So, physics dealt with either very small systems, where the total number of degrees of freedom is small, or very large systems, where the internal degrees of freedom can be treated statistically. Still, it was clear that there must exist an intermediate region between those extremes where the detailed evolution of the microscopic degrees of freedom is relevant for the macroscopic properties. It was first with the advent of computers in scientific research that this issue was first studied in the famous FPU (Fermi-Pasta-Ulam) experiment of 1954 [2].

Some decades later, mechanical systems with sizes in this interesting region between the microscopic and the macroscopic were experimentally realized. Such systems may be called *mesoscopic*<sup>1</sup>. Among these systems are NanoElectroMechanical Systems (NEMS), which combine the electronic and mechanical properties of systems on the nanoscale. In particular, low dimensional (1D and 2D) mechanical resonators are now routinely fabricated and characterized. In one or more spatial directions these systems have no extension and so no natural length scale in these directions exist (or is very small). Based on this argument, one would expect these resonators to behave nonlinearly already at low vibrational amplitudes. In fact, these resonators often display highly nonlinear behavior. This combination of mesoscopic size and strong nonlinearity, suggests that these systems contain much interesting physics.

---

<sup>1</sup>The word mesoscopic derives from the greek word mesos, meaning "intermediate". Although it is most commonly used in electronics [3], I use it in the meaning "intermediate size".

In this thesis, the nonlinear dynamics of suspended mechanical systems in one and two dimensions is characterized using classical continuum elasticity theory. Although the results obtained are generic for any low dimensional mechanical system, I specifically focus on graphene and carbon nanotubes as they are the most straightforward experimental realizations of the considered systems.

In the following sections, the reader will be familiarized with the basics of Hamiltonian dynamics as well as the basic properties of graphene and carbon nanotubes.

## 1.1 Hamiltonian dynamics

In the introductory section, I introduced linear and nonlinear systems without specifying the mathematical distinction between the two. Linear and nonlinear systems are examples of a more general class of systems, called *dynamical systems*. They are systems whose time evolution is determined by some fixed rule. At any point in time, a dynamical system is described by its *state*, which is essentially a set of numbers for the coordinates of the systems. If the system is described by  $N$  coordinates, the state can be represented as a vector in an  $N$ -dimensional space called *phase space*. For mechanical systems, which are the ones considered in this thesis, the phase space consists of all conceivable values of positions and momenta for all particles in the system. To each point in phase space corresponds a unique trajectory of the system parameters; in other words, if the state of all degrees of freedom at any specific point in time is known, the time evolution of the system is uniquely determined. A consequence of this is that phase space trajectories never cross; if they did, the time evolution would not be unique.

I shall use the following conventions: a point in phase space will be denoted by  $\mathbf{x} \equiv (p, q)$ . A trajectory in phase space will be  $\gamma(t)$ .

For physical systems, the rule determining the trajectories in phase space is Hamilton's principle. This dictates that between time  $t_1$  and  $t_2$ , the system evolves along the path that makes stationary the action

$$S = \int_{t_1}^{t_2} dt \mathcal{L}(\dot{q}, q), \quad (1.1)$$

where  $\mathcal{L}(\dot{q}, q) = T - V$  is the Lagrangian, defined as the difference between the kinetic and potential energy,  $q$  are the generalized positions of the system and  $\dot{q}$  denotes the time derivative of the coordinates. Requiring that  $S$  is stationary gives the Euler-Lagrange

equations of motion for the coordinates  $q$ ,

$$\partial_t \left( \frac{\partial \mathcal{L}}{\partial \dot{q}} \right) - \frac{\partial \mathcal{L}}{\partial q} = 0. \quad (1.2)$$

For mechanical systems, the kinetic energy is a quadratic function of  $\dot{q}$  and the potential energy is a function of  $q$ . In that case, the equations become

$$\begin{aligned} \dot{q} &= p \\ \dot{p} &= - \frac{\partial V}{\partial q}, \end{aligned} \quad (1.3)$$

where  $p = \frac{\partial \mathcal{L}}{\partial \dot{q}}$  is the generalized momentum. If the system consists of  $N$  particles, the equations are

$$\begin{aligned} \dot{q}_i &= p_i \\ \dot{p}_i &= - \frac{\partial V}{\partial q_i}, \end{aligned} \quad (1.4)$$

where  $i \in [1, N]$  labels the particles of the system. For a macroscopic system consisting of a large number of particles, this becomes a completely untractable set of, in general, nonlinear equations describing *chaotic* motion of the particles. Luckily, one is typically not interested in the exact motion of every particle in a system, but rather on some average quantity. As an example, for a swinging pendulum the interesting parameter is the motion of the center of mass of the system.

Now, we are in position to discuss the difference between linear and nonlinear systems. A linear system is a system for which the superposition principle holds, that is, if  $\gamma_1(t)$  and  $\gamma_2(t)$  are paths that satisfy the constraints set up above, then the path  $\xi(t) = \gamma_1(t) + \gamma_2(t)$  also satisfy the constraints. This principle makes it simple to construct the entire set of admissible paths, or solutions, to a dynamical system, and is the reason why so much attention has been devoted to this subclass of dynamical systems. Specifically, consider the vector field composed of the difference between two paths emanating from infinitesimally close points in phase space. If the superposition is to hold for every path, it must hold also for the path traced by this vector field. If the paths are initially very close, the equation of motion for  $\xi(t)$  can locally be written as

$$\ddot{\xi}_i = - \frac{\partial^2 V}{\partial q_i \partial q_j} \xi_j. \quad (1.5)$$

From this equation, it is clear that  $\xi_i$  satisfies the same Hamiltonian equations of motion as  $\gamma_1$  and  $\gamma_2$  when  $\frac{\partial^2 V}{\partial q_i \partial q_j}$  is independent of the position in phase space. In terms of the geometrical interpretation of phase space, a linear system is a system defined on

a potential energy manifold with everywhere constant curvature, or equivalently, the potential energy is a quadratic form. For any physical system, this is unlikely to hold globally, but it may be a good approximation locally. In particular, if the evolution of the system can be described as a small deviation from an equilibrium configuration, the potential landscape can be locally expanded to obtain linear equations. This procedure is known as linearization, and is incredibly useful for macroscopic systems. The vector field  $\xi$ , called the tangent field, is useful to illustrate the concept of Hamiltonian chaos. Consider a small portion, a volume, of phase space. A consequence of Liouville's theorem is that in Hamiltonian systems, volumes in phase space are preserved. In general, such a volume will expand in some directions and contract in other, but the total volume will always be the same. In the directions of expansion, the tangent field will diverge, which means that two points initially close in phase space will, after some time, be well separated. Consequently, nearby points in phase space do not, in general, correspond to similar dynamics. Such systems are called chaotic. Chaotic systems are characterized by the rate of separation of the tangent field, quantified by the *Lyapunov exponents*.

A final concept that aids the understanding of linear and nonlinear systems is integrability, or integrals of motion (IOM). An IOM is a number that is conserved during the evolution of the system. One example of an IOM is the total energy of a Hamiltonian system. Each IOM decreases the dimensionality of the manifold on which the phase space trajectories evolve. A completely integrable system is a system with as many integrals of motions as degrees of freedom, in which case the manifold is one-dimensional and the system is defined by a set of uncoupled equations of motion. All linear systems are completely integrable, with the integrals of motion being the individual particle (or mode) energies.

The standard way of treating weakly nonlinear systems is to start from a linear system and characterize its IOMs. The effect of small nonlinear terms in the system will then in many cases be to break the symmetry protecting the IOM causing them to depend weakly on time. The aim of standard perturbation theory is then to approximate the slow dynamics of the IOMs of the linear system.

As we have seen, the Hamiltonian description is useful if the number of degrees of freedom is small, and fluctuations of the internal degrees of freedom can be neglected. What about systems where the fluctuations themselves are of importance? This is typically the case for mesoscopic systems. Then, the above formulation must be modified.

## 1.2 Statistical mechanics

A fundamental observation of nature is that it is not time reversible. A trivial manifestation of this is playing an old VHS tape in reverse; the unphysicality of the evolution on the tape becomes painfully obvious. This irreversibility is contained in the second law of thermodynamics, which states that entropy is either constant or increases in time. At the same time, the equations of motion considered above for general Hamiltonian systems are time reversible, changing the direction of time does not alter the dynamics. As an example, consider again a movie of a pendulum swinging in a vacuum chamber. The motion of the pendulum is perpetual, and the motion will look identical whether the movie is played backwards or forwards. If the vacuum chamber is removed, the collisions between air molecules and the pendulum will act as to damp the motion of the pendulum; the amplitude of the motion decreases in time. Now, if the movie is played backward the amplitude of the pendulum will seem to increase in time; the pendulum somehow gains energy from nowhere. Suddenly, there is a clear distinction between the evolution forward and backward in time; time reversibility is broken due to the *interaction* of the system with the environment. Clearly, something happens when going from a low dimensional deterministic description as given in the preceding section to a high dimensional system (pendulum + environment) where interactions play a role.

We saw in the preceding section that a volume of phase space will contract in certain directions, and expand in other. Consequently, if one does not know the exact position of all particles but only some statistical distribution of the positions, the initial (possibly very small) phase space volume will contract and expand to a point beyond recognition. If, additionally, one is not interested in the motion of all atoms individually, but only in the statistical properties of some subsystem of the total Hamiltonian system, the equation of motions become probabilistic, or stochastic. The process of deriving these stochastic equations of motion involve projecting the full system of equations onto the subsystem of interest and performing a proper coarse-graining. For details on the procedure I refer to the excellent work by Kubo [4].

The paradigmatic example of a statistical description of a mesoscopic system is that of Brownian motion. Although this is rather far from the main course of this thesis, some aspects of statistical mechanics can be very intuitively described in the context of Brownian motion, and so I will devote a few paragraphs to it.

Brownian motion was originally observed by botanist Robert Brown in 1827, as the random motion of pollen grains suspended in water. Much later, Albert Einstein explained this motion as being due to the surrounding water molecules randomly hitting the pollen grain. If the pollen grains are freely suspended in the water, the equation of motion for

the pollen grains are

$$\begin{aligned}\dot{q} &= p \\ \dot{p} &= R(t),\end{aligned}\tag{1.6}$$

where  $R(t)$  is a force acting on the grain due to the random motion of the surrounding water molecules. If the pollen grain is stationary, one would expect that on average, the force acting on the grain is zero. If, however, the grain has a velocity, it is clear that more water molecules will hit the side of the grain facing the direction of the velocity, and the water will consequently act to damp the motion. If the water molecules move independently and uncorrelated, this term can be taken into account by including in the equations of motion a term proportional to the velocity (or momentum) of the grain,

$$\begin{aligned}\dot{q} &= p \\ \dot{p} &= -\gamma p + \xi(t)\end{aligned}\tag{1.7}$$

where  $\gamma$  is now the damping parameter and  $\xi(t)$  is a random process with some statistical properties. The inclusion of this damping term breaks the time reversal symmetry of the original problem, and is consequently an effect of the statistical description of the motion of the water molecules.

It is clear from the discussion above that there must exist a relation between the damping and the statistical properties of the random force  $\xi$ . This is given by the famous fluctuation-dissipation theorem. The fluctuation-dissipation theorem is a relation between the thermal fluctuations of a system and the dissipation, or the degree of irreversibility.

As we have seen, Hamiltonian dynamics describe well the evolution of both microscopic and macroscopic systems, where fluctuations can be disregarded. However, for systems in an intermediate range of sizes, mesoscopic systems, fluctuations play an important role in the dynamics. A lot is known about the fluctuations in linear systems. At the same time, the linearization of the equations of motion relies on the assumption that the deviation of the system from its statistical equilibrium is small. Therefore, this procedure is in general not valid for mesoscopic systems that display large fluctuations. Consequently, it is essential to be able to describe also nonlinear systems out of thermodynamic equilibrium. In the following sections, I will briefly introduce two physical realizations of mesoscopic systems that may come to aid the understanding of nonlinear nonequilibrium systems, namely graphene and carbon nanotubes.

### 1.3 Carbon based nanomaterials

The strive for smaller, faster and less energy-consuming electronic components has been central to the electronics industry for several decades. As an example, Gordon Moore noted in his 1965 paper that during the seven years preceding the paper, the number of transistors that can be integrated on a chip had doubled for each year [5], which was later modified to a doubling every two years. The fact that this exponential growth has continued to such uncanny precision that the bi-annual doubling of on-chip components is now referred to as Moore's law very clearly underlines this strive toward smaller components.

However, while the currently employed semiconducting devices reaches nanometer scales, fundamental limits to the technology prevents further miniaturization. Therefore, new materials must be used as basis for the continuing quest toward molecular sized electronics [6]. As Feynman put it in his 1959 lecture, "there's plenty of room at the bottom" [7].

Carbon, being one of the most abundant elements on Earth, would be ideal for this purpose. Not only is it the basis for all life on Earth, but the versatility of its chemical bonds results in an impressive diversity of the different forms of carbon. This allows for recycling the individual carbon atoms within an organism; the same atom can, depending on how it is bonded, be a part of the neurons firing while you are reading this thesis, or of the muscle tissue in your fingers activated as you turn the pages. This diversity is seen also in different forms of pure carbon, *carbon allotropes*. As an example, diamond is hard, transparent and insulating, while graphite is soft, opaque and conducting.

In the past decades, the possibility to apply carbon to our ever increasing technological demands have sparked a lot of interest. It has in particular focussed on a few remarkable discoveries of carbon allotropes existing on the nanoscale, starting with the so called "Buckyballs" in 1985 [8], tiny balls of carbon where the atoms are arranged in the same way as the patches of a football. Single walled carbon nanotubes, tubes of carbon in the same characteristic hexagonal, or "honeycomb" lattice as the graphite planes, were discovered in 1993 [9], although the tubular nature of carbon filaments was known much earlier [10]. Carbon nanotubes have the clear advantage over buckyballs that they can much more easily be connected to electrodes, simplifying using them in electronic applications. The next major discovery was made by Geim and Novoselov at Manchester University in 2004 [11], when they successfully isolated and characterized graphene, a single layer of graphite.

This thesis concerns mainly the theoretical description of the latter two allotropes; carbon nanotubes and graphene, based on a continuum mechanical approach.

Graphene is a two-dimensional sheet of carbon atoms in a honeycomb structure (figure 1.1). In the original experiment of Geim and Novoselov, graphene was isolated by repeatedly splitting stacked graphite layers by the use of Scotch tape [11]. This method is still frequently in use, although much current research is focussed on growing graphene chemically, to allow for industrialization of graphene growth [12].

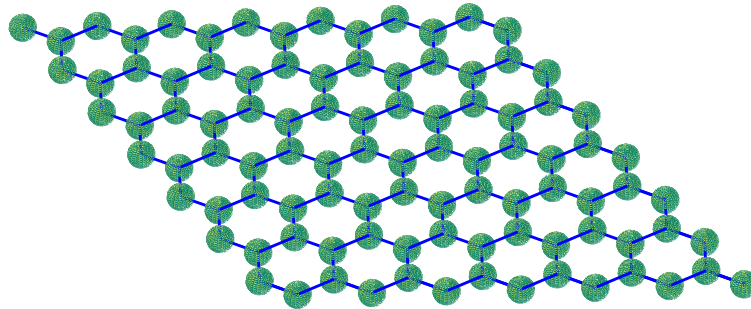


FIGURE 1.1: Schematic image of a graphene sheet, showing the carbon atoms arranged in a hexagonal lattice.

The properties of graphene differ significantly from conventional three-dimensional materials. Chemically, the bonds are constructed by hybridising two  $p$ -orbitals and one  $s$ -orbital ( $sp^2$ -hybridisation). The resulting chemical bond is referred to as a  $\sigma$ -bond, the most stable type of covalent bond. This is responsible for the remarkably high tensile strength of graphene. The remaining  $p$ -orbital may combine with free  $p$ -orbitals of neighboring carbon atoms to form a  $\pi$ -bond. These bonds are in turn what determines the electronic properties of graphene.

Among the most extraordinary features of the electronic properties of graphene is its linear spectrum close to the Fermi energy,

$$E = \pm \hbar v_F k,$$

with wave vector  $k$  measured from the so called Dirac point. The spectrum is conical with edges at the six corners of the Brillouin zone of the hexagonal lattice. Physically, this means that the velocity of the electrons,  $v = \frac{1}{\hbar} \frac{\partial E}{\partial k} = v_F$  is constant, independent of momentum, close to the Fermi energy. The Fermi velocity in graphene is  $\sim 10^6$  m/s meaning that at short distances electrons in graphene move like massless particles at about 1% of the speed of light. In fact, the electrons in this region obey the massless Dirac equation, and are therefore often referred to as massless Dirac fermions. At distances longer than the mean free path of the electrons, the charge transport is diffusive with reported electron mobilities up to  $150000 \text{ cm}^2 \text{V}^{-1} \text{s}^{-1}$  at room temperature [13, 14].

For a thorough overview of the electronic properties of graphene, the reader is referred to the review by Castro Neto et al. [1].

The unprecedented electronic properties of graphene make it a potential building block for the miniaturization of present silicon based electronics. However, graphene has a number of properties that are expected to take the industrial and societal importance of graphene even beyond that of silicon [15].

A fundamental problem in electronic applications of graphene is the lack of band gap. In recent years, there has been considerable interest in so called graphene heterostructures: layered structures of graphene and other 2D material (most notably hBN and MoS<sub>2</sub>). The lack of band gap in graphene can then be overcome by a vertical design where a few layers of hBN, MoS<sub>2</sub> or WS<sub>2</sub> are used as tunnel barriers, and graphene serves as one or both electrodes [16, 17].

The flexibility, high tensile strength and good conductive properties of graphene makes it promising for printable flexible electronics applications. In contrast to almost any other conductor, graphene is transparent which further allows for using graphene as transparent electrodes in touch screens, rollable e-paper and photovoltaic cells [18, 19].

Due to its large surface area, graphene is sensitive to its environment. This makes it useful in various sensing applications. Further, the reactivity of graphene with biological materials makes it promising for diagnostic uses. Using the shift in local electron density around adsorbed molecules, graphene can act as an extremely sensitive concentration biosensor [20, 21]. Further, utilizing the shift in conductance when a strand of DNA passes through pores in a graphene sheet, graphene can be used for fast DNA sequencing [22].

Resonators made from suspended graphene display a significant shift in frequency due to adsorbed particles, an effect that can be used for mass detection [23]. A problem arising in this kind of application is that information about the position of the adsorbed particle is typically needed to uniquely determine the mass of the particle. In particular, for a linear resonator the shift in resonance due to a light particle adsorbed near the center of the resonator is indistinguishable from the shift due to a heavier particle adsorbed closer to the rim. However, the strong nonlinearities of graphene resonators can be exploited to give information about both mass and position of an adsorbed particle [24].

Graphene additionally have potential therapeutical applications. It solubilizes and binds drug molecules and can in principle be used for drug delivery. The mechanical and chemical properties also makes it promising within tissue engineering. However, before any of these applications become viable, the possible toxicity and biodistribution of graphene in biologically relevant concentrations need to be charted [25].

Carbon nanotubes (CNT) are essentially graphene sheets rolled up into hollow cylinders. They retain the impressive tensile strength of graphene while having more easily controlled band filling. The electronic properties depend on what is known as the chirality of the atomic arrangement, and ranges from metallic to semiconducting with band gap up to several eV. [26]

The versatility of the electronic properties of CNTs make them attractive as components in applications where a strong coupling to the electronic degrees of freedom is essential. An example of this is given in chapter 5, where a CNT is used as a single electron transistor (SET). At the same time, the one-dimensional structure of CNTs makes them inferior to graphene for certain applications, for instance when a layered structure or a large surface area is preferred.

### 1.3.1 Carbon and NanoElectroMechanical Systems (NEMS)

In recent years there has been considerable interest in combining the mechanical and electrical properties of carbon allotropes on the nanoscale in so called NanoElectroMechanical Systems (NEMS). A prototypal NEMS device is depicted in figure 1.2. A graphene sheet is suspended over a trench, and is actuated by applying a voltage to the gate below it. Nanoelectromechanical systems are miniaturized extensions of the widely employed microelectromechanical systems (MEMS) developed in the 1980s. There is a wide range of enticing applications of NEMS, such as mass detectors with resolution reaching  $10^{-21}$  g [27, 28], nanoelectromechanical switches [29, 30], tunable RF resonators [31, 32], memory devices [33] and transducers actuating and detecting mechanical motion on the nanoscale [34]. Also, these structures pave the way for experimental detection of quantized mechanical motion [35–37].

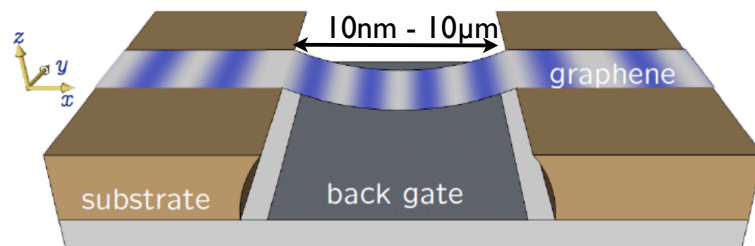


FIGURE 1.2: An archetypal graphene NEMS structure. A graphene sheet is suspended over a trench in the substrate. Mechanical motion of the graphene is induced by applying a voltage to the gate below it. The size of the structure is typically in the range 10 nm - 10  $\mu$ m.

## Chapter 2

# Continuum mechanical description of nanoresonators

The aim of this chapter is to give a short review on the elasticity theory used in the thesis. In the process, the equations of motion for a graphene sheet under external forcing are derived. The discussion follows the book of Landau and Lifshitz [38].

When an elastic body is deformed, the distance between points in the body is changed. A measure of the deformation is then the difference between the squared length element in the deformed body ( $dX_I$ ) and the undeformed body ( $dx_i$ )

$$dX_I dX_I - dx_i dx_i = \frac{\partial X_I}{\partial x_j} \frac{\partial X_I}{\partial x_k} dx_j dx_k - dx_i dx_i = \left( \frac{\partial X_I}{\partial x_j} \frac{\partial X_I}{\partial x_k} - \delta_{jk} \right) dx_j dx_k \quad (2.1)$$

where summation over repeated indicies is implied. Defining the *displacement field* as

$$u_j = X_j - x_j, \quad (2.2)$$

the difference in length elements can be written as

$$dX_I dX_I - dx_i dx_i = \left( \frac{\partial u_i}{\partial x_j} + \frac{\partial u_j}{\partial x_i} + \frac{\partial u_l}{\partial x_i} \frac{\partial u_l}{\partial x_j} \right) dx_i dx_j = 2\epsilon_{ij} dx_i dx_j. \quad (2.3)$$

Here  $\epsilon_{ij}$  is the *strain tensor*,

$$\epsilon_{ij} = \frac{1}{2} \left( \frac{\partial u_i}{\partial x_j} + \frac{\partial u_j}{\partial x_i} + \frac{\partial u_l}{\partial x_i} \frac{\partial u_l}{\partial x_j} \right). \quad (2.4)$$

Carbon based nanomaterials have a hexagonal atomic structure. The hexagonal lattice is the maximally symmetric lattice and implies a symmetry between strains in different

directions in the structure. Consequently, the free energy density describing a deformed carbon based nanostructure is given by only two material parameters  $\lambda$  and  $\mu$ , called the Lamé parameters. These parameters relate the on- and off-diagonal terms in the strain to the free energy density according to

$$F = \frac{\lambda}{2} \epsilon_{ii} \epsilon_{jj} + \mu \epsilon_{ij} \epsilon_{ij}. \quad (2.5)$$

The internal stresses in the structure are given by the stress tensor,

$$\sigma_{ij} = \frac{\partial F}{\partial \epsilon_{ij}}. \quad (2.6)$$

This gives a linear relation between the strain and the stress in the material, and it is a two-dimensional generalisation of Hooke's law. The free energy density can be written explicitly in cartesian coordinates as

$$F = \frac{1}{2} \sigma_{ij} \epsilon_{ij} = \left( \frac{\lambda}{2} + \mu \right) (\epsilon_{xx}^2 + \epsilon_{yy}^2) + \lambda \epsilon_{xx} \epsilon_{yy} + 2\mu \epsilon_{xy}^2, \quad (2.7)$$

Denoting the displacement fields by

$$u_x = u(x, y), \quad u_y = v(x, y), \quad u_z = w(x, y), \quad (2.8)$$

the components of the strain tensor are, to lowest nonvanishing order in the displacement fields,

$$\begin{aligned} \epsilon_{xx} &= \partial_x u + \frac{1}{2} (\partial_x w)^2, \\ \epsilon_{yy} &= \partial_y v + \frac{1}{2} (\partial_y w)^2, \\ \epsilon_{xy} &= \frac{1}{2} (\partial_y u + \partial_x v + \partial_x w \partial_y w). \end{aligned} \quad (2.9)$$

Higher order terms of the in-plane displacements have been omitted. This approximation will be denoted the membrane approximation, and is the main approximation of interest in this thesis. Note that the nonlinearities in the strain appear only through the out-of-plane deformation  $w$ . Further, there is no linear term in  $w$ , so the response is expected to be highly nonlinear even for small deformations. Finally, in this model, there is no external parameter that sets the size of the nonlinearity; it is an intrinsic feature of these structures. It is very important that this nonlinearity arises not due to a nonlinear force between the atoms, but is simply a consequence of Pythagoras' rule. The nonlinearity is therefore said to be *geometrical*.

However, there is one parameter left to be discussed in this context, namely the geometry of the sample. For a carbon nanotube this is irrelevant, but the additional dimension of graphene sheets makes this an important issue. Therefore, I now introduce the two main geometries of interest in this thesis, the nanobeam and the nanodrum (fig 2.1). The nanobeam is a rectangular graphene sheet with two free edges and two fixed edges. The nanodrum, on the other hand, is a circular sheet with its entire boundary fixed.

Nanobeams are the natural choice when the dynamics is to be coupled to electronic degrees of freedom. As the supports of the nanobeam are separated in space, a voltage can be applied over the length of the beam effectively using the nanobeam as a conducting channel. This is more challenging for the drum geometry.

On the other hand, the beam geometry suffers from mechanical drawbacks. The tension in the sheet is often nonuniform, which makes the oscillation modes less well-defined [39]. Further, they may possess edge modes on the free edges which degrade the quality factor of the resonator [40].

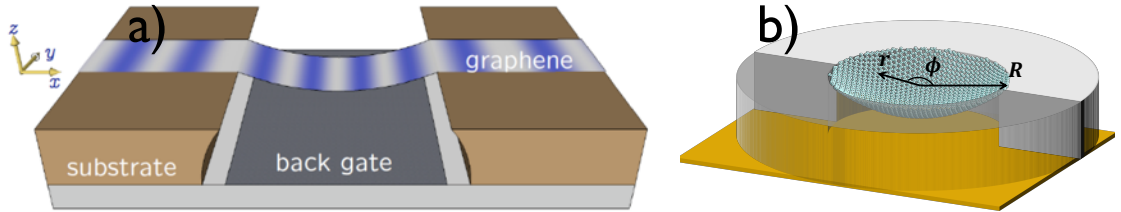


FIGURE 2.1: The geometries considered in this thesis. a) Beam geometry, b) Drum geometry.

Resonators made from exfoliated graphene usually have some residual tension  $T_0$ , which introduces a linear term in the equations of motion. Further, in NEMS applications the resonator typically oscillates around a static equilibrium shape  $\bar{w}$  induced by a static load. The analysis of the continuum mechanical description of graphene resonators therefore need to take both these effects into account.

A further approximation will be employed in all models of this thesis. The time scale of the in-plane dynamics and the out-of-plane dynamics is well separated in graphene resonators. The time scale for the in-plane dynamics is set by  $l\sqrt{\rho_G/T_1}$ , where  $l$  is a typical size of the suspended domain,  $T_1 = \lambda + 2\mu$  and  $\rho_G$  is the mass density of graphene. The time scale for the out-of-plane dynamics is similarly set by  $l\sqrt{\rho_G/T_0}$ , where  $T_0$  represents the residual stress in the resonator. Since  $T_0/T_1$  is of the order  $10^{-3}$  for graphene resonators made from exfoliated graphene, the in-plane dynamics is much faster than the out-of-plane dynamics. In other words, the in-plane field will follow the

out-of-plane field adiabatically, and are therefore removed from the dynamics by setting  $\partial_t^2 u_i = 0$ .

The equations of motion for a nanobeam are derived and analyzed in appendix A. The equations of motion can be reduced to a set of coupled differential equations describing the evolution of the oscillation modes  $q_n$  driven by a pressure  $p_z \cos \omega t$ ,

$$\ddot{q}_n + \tilde{\omega}_n^2 q_n + \delta\omega_n^2 \left( q_n + \frac{8w(0)}{n^2\pi^2} \langle \phi_n \rangle \right) = \langle p_z \phi_n \rangle \cos \omega t, \quad (2.10)$$

with  $\tilde{\omega}_n^2 = n^2\pi^2 (1 + \langle \bar{w}_x^2 \rangle)$  and  $\delta\omega_n(t)^2 = n^2\pi^2 (\sum_m q_m \langle 2\bar{w}_x \partial_x \phi_m \rangle + \pi^2 \sum_m m^2 q_m^2)$ ,  $w(0)$  is the maximal deflection of the static equilibrium shape,  $\phi_i$  is the  $i$ :th mode shape,  $\langle \cdot \rangle$  denotes spatial integration over the beam, subscript  $x$  denotes spatial derivative and  $\bar{w}$  is the static equilibrium shape of the resonator. This equation is written in dimensionless form, the explicit form of which is also given in appendix A.

The derivation shows that the presence of a static deformation gives rise to a uniform renormalization of the stress in the sheet. Further, it turns out that in the absence of a static deformation, the modes are coupled only parametrically, i.e. through fluctuations in the mode frequencies.

## 2.1 Equation of motion for a nanodrum

The continuum mechanical description of nanodrums is investigated in detail in Paper I. I will here summarize the most important results of that paper. The Föppl-von Kármán equations for the drum geometry read

$$\rho_0 \ddot{u}_r - [\partial_r \sigma_{rr} + r^{-1} \partial_\phi \sigma_{r\phi} + r^{-1} (\sigma_{rr} - \sigma_{\phi\phi})] = 0, \quad (2.11)$$

$$\rho_0 \ddot{u}_\phi - [\partial_r \sigma_{r\phi} + 2r^{-1} \sigma_{r\phi} + r^{-1} \partial_\phi \sigma_{\phi\phi}] = 0, \quad (2.12)$$

$$\rho_0 \ddot{w} - r^{-1} [\partial_r (r \sigma_{rr} \partial_r w + \sigma_{r\phi} \partial_\phi w) + \partial_\phi (\sigma_{r\phi} \partial_r w + r^{-1} \sigma_{\phi\phi} \partial_\phi w)] = P_z(r, t), \quad (2.13)$$

where  $P_z$  is an externally applied pressure. As in the case of the nanobeam, the equations can be cast in the form of a coupled mode equation. To derive these equations, the in-plane dynamics is eliminated adiabatically and the following scaled variables are introduced,

$$\tilde{r} = \frac{r}{R}; \quad \tilde{t} = \frac{\sqrt{\epsilon} c_L}{R} t; \quad \tilde{w}^2 = \frac{1}{2} \frac{w^2}{R^2 \epsilon}; \quad \tilde{E} = \frac{E}{2\epsilon^2 c_L^2 \rho_G R^2}; \quad \Phi_z = P_z R / T_0, \quad (2.14)$$

where  $c_L^2 = T_1 / \rho_G$  is the longitudinal speed of sound in graphene,  $\epsilon = T_0 / T_1$  is the pre-strain of the sheet,  $R$  is the radius of the drum,  $P_z$  is the external pressure and  $\rho_G$

is the mass density of graphene. Explicit calculations show that the equations of motion have the form

$$\partial_\tau^2 q_n + \tilde{\omega}_n^2 q_n + \sum_{j=1}^{\infty} \sum_{k \geq j}^{\infty} B_{njk} q_j q_k + \sum_{j=1}^{\infty} \sum_{k \geq j}^{\infty} \sum_{l \geq j}^{\infty} W_{nj;kl} q_j q_k q_l = \langle \Psi_n^* \delta \Phi_z \rangle, \quad (2.15)$$

where  $\phi_n^*$  is the  $n$ :th mode function and  $\delta \Phi_z$  is the time dependent part of the external pressure.

The quadratic coupling  $B_{nij}$  arises due to the broken symmetry when the membrane fluctuates around a static curved equilibrium shape, and vanishes if the fluctuations occur around a flat, unbiased equilibrium. The cubic coupling matrix  $W_{nj;kl}$  is dense, and has a permutation symmetry in the indices  $n \leftrightarrow j$  and  $k \leftrightarrow l$ . To highlight this symmetry, the matrix is denoted as  $W_{nj;kl}$ .

In contrast to the beam geometry, the modes are coupled not only parametrically. Instead, a single mode can be driven by the presence of other vibrational modes in the system. This feature of the drum resonator will be employed in chapter 3, where the thermalization of graphene resonators due to mode coupling is investigated.

Another difference is that a static deformation due to a homogeneous pressure no longer results in a homogeneous increase in the resonator stress. The inhomogeneity of the stress renormalizes the frequencies of the modes, and gives rise to nontrivial frequency crossings when the static pressure is increased.

### 2.1.1 Equations of motion for carbon nanotubes; effect of bending

Readers familiar with structural mechanics may have noted that the boundary conditions considered in the previous section are different from what is ordinarily encountered in that context. In particular, one usually requires information also regarding the derivatives of the displacement field at the boundary. The reason for this is that typically, there is an energy cost associated with bending a structure, while in the preceding section only the energy cost of stretching was considered. Macroscopically, the origin of this energy cost is that for a bent structure the convex side will be slightly stretched, while the concave side will be compressed. This mechanism will not be present in atomically thin structures such as graphene monolayers. On the atomistic scale, bending changes the bond angles between carbon atoms, which will also cost energy. This energy is, however, in most applications very small compared to the stretching energy, and so it will be ignored for graphene structures for a large part of the thesis. The issue of bending rigidity in graphene mono- and multilayer structures is revisited in chapter 4.

For carbon nanotubes (CNT:s), the situation is different. When bending a CNT, it is clear that one side of the tube will be stretched, while the other is compressed. Therefore, bending plays a more significant role for CNT:s than for graphene. The free energy density of a CNT is, for small deformations

$$F = \frac{\kappa}{2} (w_{xx})^2 + \frac{T_1}{2} (u_x^2 + u_x w_x^2 + w_x^4/4), \quad (2.16)$$

where  $\kappa$  is the bending rigidity. The appearance of a term quadratic in the flexural motion in the free energy density implies that the equation of motion will be linear for small amplitudes. In this regime, mode coupling will be of minor importance and the motion of the nanotube can be well modeled by considering the dynamics of a single mode. In chapter 5, this model for the CNT motion is coupled to a quantum dot as an interesting example of how a strong coupling between mechanical motion and electronic degrees of freedom can be achieved.

## 2.2 Actuated nanoresonators

In applications, nanoresonators are actuated by an external field. In this thesis, the actuation mechanism is electrostatic. The resonator is suspended over a back gate. When a voltage is applied to the back gate, the resulting electric field between the back gate and the suspended nanostructure causes charge to accumulate on both surfaces, much as in a regular capacitor. This charge accumulation generates a force between the gate and the resonator, which in turn causes the resonator to move.

As a first approximation for the case of a suspended graphene sheet, consider two static, parallel plates separated by a distance  $d$ . The voltages on the two plates are  $\pm V/2$ , respectively. The electric field between the plates is homogeneous and given by  $E_z = V/d$ . From Gauss law it follows that the charge on the plates are given by  $Q = \pm \epsilon_0 AV/d$ , where  $\epsilon_0$  is the vacuum permittivity. The proportionality constant between the charges and the applied voltage is called the *capacitance* of the system. The force between the plates is given by

$$\mathbf{F} = F_z \hat{z} = \frac{1}{2} \frac{\partial C}{\partial z} V^2 \hat{z}. \quad (2.17)$$

Note that taking the voltage  $V$  to be oscillating with frequency  $\omega$ , the force oscillates at the double frequency,  $2\omega$ . The reason for this is that reversing the sign of the voltage does not reverse the sign of the force; the opposing charges on the two plates will still attract.

For simplicity, I will consider an actuation that only affects the fundamental mode. The effective equation of motion for the fundamental mode of the resonator becomes

$$\ddot{q}_0 + \omega_0^2 q_0 + \alpha q_0^3 = A^{-1} \langle F_z \phi_0 \rangle, \quad (2.18)$$

where  $A$  is the resonator area,  $\omega_0 = (\pi/l)\sqrt{T_0/\rho_G}$  for a nanobeam,  $\omega_0 = (\xi_{0,0}/R)\sqrt{T_0/\rho_G}$  for a nanodrum where  $\xi_{0,0} \approx 2.4$  is the first zero of the zeroth order Bessel function, and  $\alpha = (c_L^2/2)(\pi^4/l^4)$  for a nanobeam and  $\alpha \approx (2/3)(c_L^2/2)\langle r(\partial_r \phi_0)^4 \rangle$  for a drum.

The effect of this force acting on the graphene sheet will be that the graphene sheet starts to oscillate. However, when the graphene moves, the distance separating the graphene and the back gate will change, effectively changing the force acting on the graphene. To estimate this effect, consider a voltage signal consisting of a static part and a time varying part,  $V(t) = V_{dc} + V_{ac}(t)$ ,  $V_{dc} \gg V_{ac}$ . To a first approximation the force is given by

$$F_z[x, y, t, w] = \frac{\epsilon_0}{2(d-w)^2} [V_{dc} + V_{ac}(t)]^2, \quad (2.19)$$

where  $w$  is the deviation from the equilibrium position of the graphene sheet,  $d$  is the distance to the backgate and  $\epsilon_0$  is the vacuum permittivity. This force may be Taylor expanded around the static equilibrium of the resonator to obtain the renormalization of the resonance frequency,

$$\delta\omega_{el}^2 = \frac{\epsilon_0}{\rho d^3} V_{dc}^2, \quad (2.20)$$

as a consequence of the electrostatic interaction between the graphene and the back gate. Additionally, the mechanical nonlinearities gives a renormalisation of the frequency  $\delta\omega_{mech}$  of opposite sign. It is worth noting, that when  $\omega_0^2 - \delta\omega_{el}^2 + \delta\omega_{mech}^2 < 0$  where  $\omega_0$  is the frequency of the fundamental mode, the structure is unstable and the graphene sheet will irreversibly "snap in" to the back gate.

The shift of resonance frequency with static gate voltage, the so called tuning curve, is a characteristic feature of NEMS devices. In figure 2.2, the tuning curve is reported for both a nanobeam of length  $l = 500$  nm and a nanodrum of radius  $R = (\xi_{0,0}/\pi)l$ , chosen to have the same non-renormalized frequency as the beam. The sheets are suspended 300 nm above the backgate, and the initial strain is taken to be  $T_0/T_1 = 0.001$ .

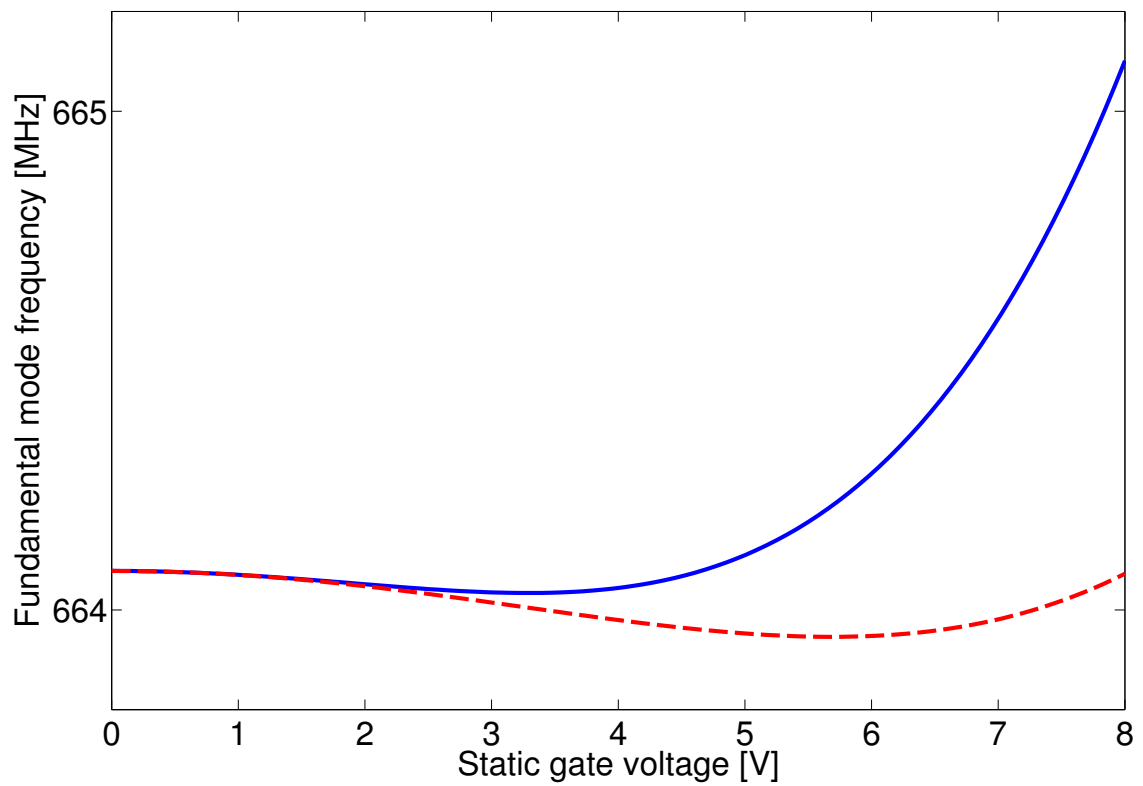


FIGURE 2.2: The renormalized resonance frequency as a function of gate voltage for a drum (dashed line) and beam (full line) with parameters as given in the main text. The drum displays less mechanical stiffening compared to the beam.

## Chapter 3

# Dissipation and relaxation in graphene resonators

All truth is crooked, time itself is a  
circle

---

Friedrich Nietzsche

When a mechanical subsystem, such as a NEMS-resonator, is put out of equilibrium one expects that the energy of the resonator decays and relaxes to the thermal equilibrium of its environment. The time scale at which this happens defines the dissipation rate, and is a fundamental limiting factor for the application of NEMS-devices. Understanding the processes that lead to relaxation is therefore of key importance.

The standard way of describing relaxation of a subsystem toward thermal equilibrium is provided by the Caldeira-Leggett model [41, 42], in which the subsystem is coupled to a "bath" of linear harmonic oscillators. By bath one means a set of  $N$  oscillators that are in thermal equilibrium with each other, with  $N$  large enough that the distribution of energies among the oscillators is well described by its statistical properties. In the limit that  $N \rightarrow \infty$ , this model describes an irreversible relaxation of the subsystem towards the thermal equilibrium of the bath. In section 3.2, the relaxation of the fundamental mode of a graphene resonator is described in the context of the Caldeira-Leggett model.

However, the Caldeira-Leggett model reveals some deep underlying problems in the classical statistical mechanics description of the physical world, without really providing any answers. For instance, the dynamics of any physical system can be described by a Hamiltonian. Hamiltonian dynamics is inherently time-reversible, yet the relaxation toward thermal equilibrium is irreversible. In other words, how can one reconcile the

first law of thermodynamics, stating that the energy of any closed system is constant, thereby implying reversible motion, with the second law, implying an irreversible increase in entropy? One can gain a heuristic understanding of this by considering Poincaré recurrences. Any Hamiltonian system evolves along the closed geodesics of an  $(N - 1)$ -dimensional manifold in  $N$ -dimensional phase-space [43]. In other words, after a finite amount of time, the system passes through the same point in phase space; the system returns to its initial condition. The time this takes is called the Poincaré recurrence time. The more degrees of freedom a system has, the larger phase space will be. As a consequence, the probability for this type of return decreases very quickly with the dimensionality of the system, and so for high-dimensional systems only a finite part of the geodesic will be explored within a physically reasonable amount of time. This makes the dynamics appear irreversible, without being so in a rigorous sense.

The second question regards the requirements of a physical system to display a thermal equilibrium. The concept of a thermal equilibrium relies on the assumption that statistical properties of a system can be obtained without knowing the details of the high-dimensional trajectories involved. In particular, if the trajectories uniformly covers the constant energy manifold on which the system is defined, time integrations over individual trajectories can be replaced by a phase space integral over the manifold. This is the concept of ergodicity, which lies at the heart of classical statistical mechanics [44]. The system of uncoupled harmonic oscillators employed in the Caldeira-Leggett model is for instance not ergodic in this sense, as additional integrals of motion restricts the geodesics on the manifold to only a subspace of it. Therefore, the geodesics do not cover the entire manifold in this case. Further, the very same argument that resolved the issue of irreversibility in reversible systems seem to cause a contradiction now since for high-dimensional systems, only a finite part of the manifold can be covered within a physical time. Therefore, for a thermal equilibrium to be reasonably defined, not only ergodicity is required, but also that large, separated portions of the manifold is covered within finite time. This is called mixing, and is typically seen in chaotic systems. There has been significant research on the relation between chaotic motion in Hamiltonian systems and statistical mechanical properties of the system.

A natural question that arises is then, what are sufficient and necessary conditions on the Hamiltonian for the system to relax toward a uniquely defined thermal equilibrium? How do these conditions scale with the dimensionality of the system? These questions were posed by Fermi, Pasta and Ulam (FPU) in their famous computer experiment of 1955 [2], and has been an active area of research ever since. The status of this research is summarized in section 3.1, and in section 3.3 the idea of experimentally investigating those questions in graphene resonators is proposed and analyzed. For excellent reviews on the FPU problem I refer the reader to [45–47] and the recent book [48].

### 3.1 FPU problem

The model system employed by FPU in their investigation of relaxation in finite-dimensional systems was a set of coupled, nonlinear oscillators. The Hamiltonian they considered was

$$H = \frac{1}{2} \sum_n (p_n^2 + \omega_n^2 q_n^2) + \frac{\alpha}{3} \sum_n (q_{n+1} - q_n)^3 + \frac{\beta}{4} \sum_n (q_{n+1} - q_n)^4, \quad (3.1)$$

where  $\alpha$  and  $\beta$  were considered small perturbations to the linear system of uncoupled oscillators. The cases  $\alpha = 0$  and  $\beta = 0$  are called the FPU- $\beta$  problem and the FPU- $\alpha$  problem, respectively. According to a theorem by Fermi, nonlinear systems generally do not have additional integrals of motion aside the energy, and so the system is expected to be ergodic for arbitrarily small perturbations. Based on this, the expectation by FPU was that the system would display relaxation toward a thermal equilibrium determined only by the energy of the system. The time scale of the relaxation was expected to increase as the perturbation parameter decreased and become infinite in the limit  $\alpha, \beta \rightarrow 0$ . Much to their surprise, the system instead displayed quasiperiodic motion, and showed no signs of equipartition. This very innocent computer experiment spawned an enormous amount of research on nonlinear Hamiltonian dynamics, the most important results of which I will try to summarize here.

A possible explanation to the paradoxical observations of Fermi, Pasta and Ulam was provided in 1965 by Kruskal and Zabusky [49]. They considered an equation describing the short-time evolution of the FPU chain in the continuum limit, namely the Korteweg-de Vries (KdV) equation,

$$u_t + uu_x + u_{xxx} = 0. \quad (3.2)$$

This equation is a certain continuum limit of the FPU equations obtained by taking  $\beta = 0$  (FPU- $\alpha$  model), and describes the evolution of a combination of the momentum and displacement field of the FPU chain. For a derivation of this equation I refer to [50]. Kruskal and Zabusky numerically found that certain solitary waveforms (solitons) traveled through the chain without losing their shape. This result sparked the development of the mathematical field of solitons and integrable nonlinear systems. However, although not explicitly stated in the original paper, this equation approximates the FPU- $\alpha$  model only on a short time scale, and the results obtained by Zabusky and Kruskal therefore failed to give a complete explanation of the FPU results.

A year later, Izrailev and Chirikov [51] found evidence of a critical energy, below which the system displayed regular motion. Above the critical energy, an approach to equipartition was observed. A heuristic theoretical explanation was also provided in the context

of the Kolmogorov-Arnold-Moser theory. In essence, one may say that the presence of a perturbing nonlinear term in the Hamiltonian distorts the constant energy manifold. For a given value of the perturbation parameter, this distortion vanishes in the limit  $E \rightarrow 0$ . Thus, for small energies the geodesics remain almost unchanged. In particular, the constants of motion are destroyed only locally close to resonances. They conjectured that irreversible energy sharing implied chaotic motion, which they attributed to a resonance overlap.

Thus, the understanding of the FPU problem was the following: initially, the system quickly relaxes to a superposition of normal modes, the stable solitons found by Zabusky and Kruskal. For low energies, these solitons are stable, but for larger energies the solitons constitute a metastable state and eventually break down and the system relax toward equipartition.

Israeliv and Chirikov went even further by noting that in the "thermodynamic limit"  $N \rightarrow \infty$ , where  $N$  is the number of oscillators, the energy threshold vanished, and they therefore drew the conclusion that the "FPU-paradox" was irrelevant for the general problem of ergodicity in statistical mechanics. However numerical evidence shows the opposite behavior; the persistence of the metastable state in the limit of large oscillator chains. In particular, the threshold for equipartition seemed to occur at the same value of energy density or specific energy of the system  $\epsilon \equiv E/N$ , regardless of system size [52]. These observations steered the focus of the FPU problem in the direction it has had ever since; namely, does the lack of equipartition observed by FPU persist in the thermodynamic limit, and what implications would this have for classical statistical mechanics?

It is now generally recognized that a second threshold exist, akin to a phase transition, below which the phase space is mostly regular, with small stochastic islands close to resonances, and above which most of phase space consists of chaotic orbits [53]. For low energies, the dominating mechanism for energy redistribution is a slow diffusion along resonances, so called Arnold diffusion, while for higher energies diffusion across resonances gives a much faster equilibration. This threshold is seen as a cross-over in the scaling of the largest Lyapunov exponent, a measure of the rate of separation of two initially nearby points in phase space. The observation of this second threshold led to a very interesting reformulation of classical mechanics in terms of Riemannian geometry [54–58]. In particular, using these results the strong stochasticity threshold for large Hamiltonian systems could be evaluated analytically [59].

Consequently, the parameters typically studied in the context of coupled oscillator chains are the scaling of the largest Lyapunov exponent,  $\lambda(\epsilon)$ , and the scaling of the equilibration time  $T_{eq}(\epsilon)$ , where  $\epsilon$  is the specific energy,  $\epsilon \equiv E/N$ .

### 3.2 Dissipation in graphene resonators coupled to a medium

In this section, the equations of motion for a graphene sheet coupled to a medium are derived and analyzed. The coupling will, as was discussed above, introduce dissipation of the vibrational energy of the graphene sheet.

If the graphene is suspended in a gas (air, for instance), the gas molecules will collide with the vibrating sheet, leading to a direct coupling to the flexural motion of the sheet. This will induce regular, viscous damping. A more interesting scenario occurs when the external bath couples to the strain. Then, the coupling will affect the flexural motion indirectly through the in-plane field. This type of coupling occurs for instance for electrons coupling to the deformation potential of strained graphene, or for phonon-phonon coupling between graphene and the supporting substrate. This type of coupling, as I will demonstrate, gives rise to a qualitatively different type of damping, where the dissipation rate depends on the flexural mode amplitude.

I will consider the case when the in-plane motion of the graphene is coupled to a linear elastic medium. Equations of motion are derived for a general geometry, and the specific cases of a nanobeam and a nanodrum are considered separately.

Consider a graphene sheet suspended in a region  $\Omega$ , otherwise connected to an elastic substrate. Assuming that the interaction between the graphene sheet and the substrate is harmonic in the displacement, the Hamiltonian of the system is

$$H = H_G + H_m + \frac{1}{2} \sum_i \lambda_{i\Omega} (u_i - s_{i,z=0})^2, \quad (3.3)$$

where  $H_G$  and  $H_m$  are the uncoupled graphene and medium Hamiltonians,  $s_{i,z=0}$  is the displacement field of the substrate at the surface  $z = 0$ , and the coupling parameters  $\lambda_{i\Omega}$  are non-vanishing only outside the suspended domain  $\Omega$ .

The equations of motion for the subsystems are

$$\begin{aligned} \rho_G \ddot{\vec{u}} &= \nabla \cdot \vec{\sigma} + \lambda_\Omega (\vec{u} - \vec{s}_{\parallel,z=0}), \\ \rho_G \ddot{w} &= \nabla \cdot (\vec{\sigma} \nabla w), \\ \rho_S \ddot{\vec{s}} &= \mu \nabla^2 \vec{s} + (\lambda + \mu) \nabla (\nabla \cdot \vec{s}) - \lambda_\Omega (\vec{u} - \vec{s}_{\parallel,z=0}) - \lambda_{z\Omega} (w - s_{z,z=0}), \end{aligned} \quad (3.4)$$

where  $\vec{s}_{\parallel,z=0}$  are the in-plane displacements of the substrate on the surface. The response of the substrate at the surface can be written in terms of a response function  $M_{ij}$ ,

$$\tilde{s}_i(\vec{x}, z=0, \omega) = - \int d\vec{x}' M_{ij}(\vec{x} - \vec{x}', \omega) \sigma_{jz}(\vec{x}', \omega), \quad (3.5)$$

where  $\sigma_{jz}(\vec{x}', \omega) = \lambda_\Omega(u_j - s_{j,z=0})$  is the stress at the surface of the substrate.

The equation of motion for the fundamental mode dynamics resulting from this coupling is derived in appendix B. The dynamics of the fundamental mode in the rotating wave approximation  $q_1$  can be written

$$i\omega q_1 + \frac{1}{2}(\tilde{\omega}_0^2 - \omega^2)q_1 + \frac{3}{8}\frac{\tilde{\alpha}}{m}|q_1|^2q_1 + i\frac{1}{2m}\gamma\omega q_1 + i\frac{1}{8m}\eta\omega|q_1|^2q_1 = \frac{f_0}{2m}\langle\phi\rangle, \quad (3.6)$$

where  $\tilde{\omega}_0$  is the renormalised resonance frequency of the sheet,  $\tilde{\alpha}$  is the renormalised Duffing parameter,  $\gamma$  and  $\eta$  correspond to the linear and nonlinear damping,  $\phi = \phi(x)$  is the fundamental mode shape,  $\omega$  is the driving frequency,  $m$  is resonator mass and  $f_0$  is the driving strength. Following Lifschitz [60], the following dimensionless quantities are investigated,

$$\delta = \frac{\eta|q_1|^2}{4\gamma} = \frac{\text{Im}\{\langle(\nabla\phi)^T\tilde{\sigma}^u(2\omega)\nabla\phi\rangle\}|q_1|^2}{8\text{Im}\{\langle(\nabla\phi)^T\tilde{\sigma}^u(\omega)\nabla\phi\rangle\}q_0^2}$$

$$\tilde{\eta} = \frac{\eta\omega}{\tilde{\alpha}}. \quad (3.7)$$

The first of the dimensionless quantities measures the relative magnitude of the linear and nonlinear damping. This is determined by the ratio of overlap integrals of the mode shapes  $\phi$  and the frequency components of the in-plane stress field  $\tilde{\sigma}^u(\omega)$ , and by the ratio between the vibrational amplitude  $q_1$  and the static displacement of the graphene sheet  $q_0$ . For a small static displacement, it is therefore expected that the nonlinear damping dominates the dissipation caused by this mechanism. The second quantity measures the relative importance of the two nonlinearities in the equation. For  $\tilde{\eta} < \sqrt{3}$ , the well-known bifurcation of the Duffing equation is present, while for  $\tilde{\eta} > \sqrt{3}$  this bifurcation vanishes [60]. This is a purely geometrical factor, apart from the weak dependence of  $\omega$  on the static deformation of the graphene.

As a measure of the total dissipation due to this mechanism, we consider the quality factor, defined as

$$Q = \frac{\tilde{\omega}_0\bar{E}}{\dot{E}}, \quad (3.8)$$

where  $\bar{E}$  is the energy of the subsystem of interest, averaged over one period. Here, the concern is the damping of the out-of-plane motion. The energy  $E$  is consequently the part of the energy of the graphene related to the out-of-plane motion. In the rotating frame, it is given by

$$E = m\tilde{\omega}_0^2|q_1|^2 + \frac{1}{4}\tilde{\alpha}|q_1|^4 \quad (3.9)$$

The expression for the quality factor becomes, retaining only terms quadratic in  $q_1$ ,

$$Q^{-1} = \tilde{\gamma} \frac{1 + \delta}{1 + (3/16)|\tilde{q}_1|^2}, \quad (3.10)$$

where the dimensionless variables

$$\tilde{q}_1 = q_1 \sqrt{\frac{\tilde{\alpha}}{m\omega^2}}; \quad \tilde{\gamma} = \gamma/(m\omega), \quad (3.11)$$

are introduced.

This result for the quality factor is valid in the limit  $T = 0$ . For  $T > 0$  the thermal motion of the substrate must be taken into account when deriving the equations of motion for the suspended graphene.

The terms entering equation (3.10) depend on the geometry of the suspended domain, and on the elastic properties of the supporting substrate.

To get quantitative results, a suspended beam and a circular drum coupled to SiO<sub>2</sub> has been considered. The structures are assumed to be actuated electrostatically. To get quantitative results, specific mode shapes must be chosen. The mode shapes are determined by the geometry of the suspended region, and are chosen according to the fundamental mode shapes of a beam and a drum,

$$\begin{aligned} \phi_{\text{Beam}} &= \sqrt{2} \cos\left(\frac{\pi x}{l}\right) \\ \phi_{\text{Drum}} &= \frac{J_0\left(\frac{\xi_{0,0} r}{R}\right)}{J_1(\xi_{0,0}/R)}. \end{aligned} \quad (3.12)$$

Assuming the structures to be electrostatically actuated, this also allows for calculation of the static displacement  $q_0$ ,

$$\begin{aligned} q_{0,\text{Beam}} &\approx -\sqrt{2} \frac{l^2 \epsilon_0 V_{\text{dc}}^2}{\pi^3 T_0 d^2} \\ q_{0,\text{Drum}} &\approx -\frac{R^2 \epsilon_0 V_{\text{dc}}^2}{\xi_0^3 T_0 d^2}. \end{aligned} \quad (3.13)$$

To find the amplitude of the vibrational motion, I further define

$$\tilde{f} = \frac{f}{\omega^3} \sqrt{\frac{\tilde{\alpha}}{m^3}}, \quad (3.14)$$

where  $f$  is the amplitude of the oscillating force actuating the vibrational motion, projected onto the fundamental mode shape. Then, following [61], the maximal amplitude

$|\tilde{q}_{1,\max}|$  of the vibrational motion of the Duffing oscillator is given by the relation

$$\tilde{f} = |\tilde{q}_{1,\max}| (4\tilde{\gamma} + |\tilde{q}_{1,\max}|^2). \quad (3.15)$$

The last piece needed to calculate the parameters of the equation is the response function of the substrate, which is taken from [62, 63].

It is interesting to note that the phonons emitted to the substrate from the oscillations of the graphene are quite different for the two geometries. For the circular geometry the graphene will act as a monopole, emitting phonons in a radially symmetric fashion. In contrast, the beam structure will act as a dipole, with a radiation pattern with strong directionality. This also influences the frequency dependence of the emitted radiation; it is well known that the power emitted by a dipole scales as  $P \sim \omega^4$ , while the power from a monopole scales as  $P \sim \omega^2$  [64]. Since the source of the emitted radiation is the vibrational energy of the resonators, the power received by the substrate must equal the dissipated power of the resonator. Since the dissipated power of a harmonic oscillator scales as  $\omega\gamma$ , it is clear that the imaginary part of the overlap integrals  $\langle (\nabla\phi)^T \tilde{\sigma}^u(\omega) \nabla\phi \rangle$  must scale with  $\omega$  for circular drums, and with  $\omega^3$  for beams. This is confirmed in figure 3.1, where this overlap is plotted for both geometries as a function of frequency.

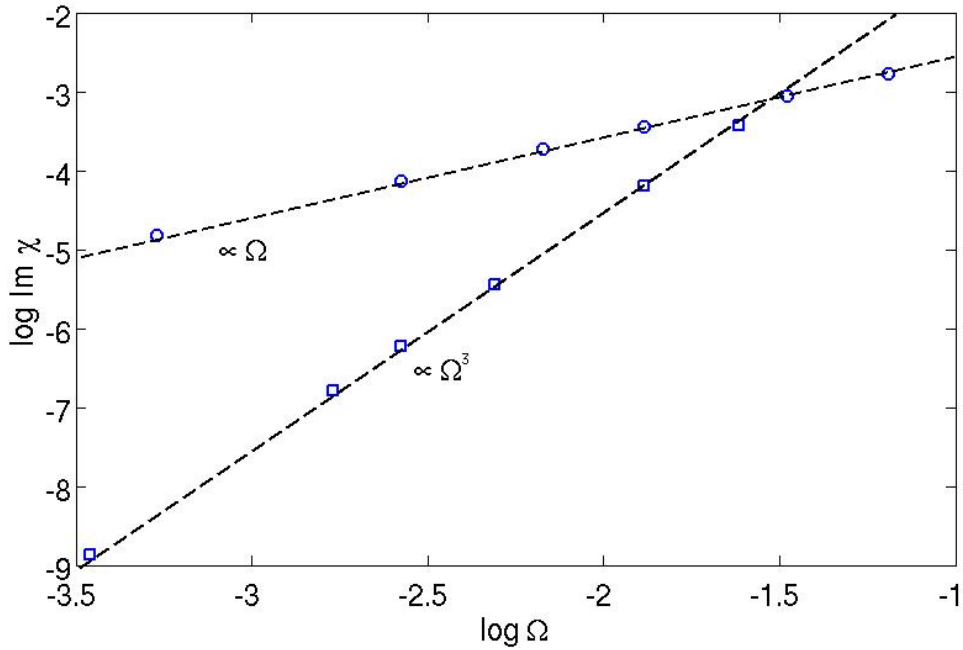


FIGURE 3.1: The scaling of the imaginary part of the overlap integrals for beams (squares) and drums (circles) with frequency in logarithmic scale. The dashed lines correspond to least square fits proportional to  $\Omega^3$  for the beams and  $\Omega$  for the drums

This scaling of the overlap integrals implies a certain scaling of the quality factor. Writing

$$Q^{-1} = \tilde{\gamma}(1 + \delta), \quad (3.16)$$

valid for  $|q_{1,\max}| \ll 1$ , it is clear that the quality factor will be  $Q_{\text{LD}}^{-1} = \tilde{\gamma}$  for  $\delta \ll 1$  and  $Q_{\text{NLD}}^{-1} = \tilde{\gamma}\delta = \frac{1}{4}\tilde{\eta}|\tilde{q}_{1,\max}|^2$  for  $\delta \gg 1$ .

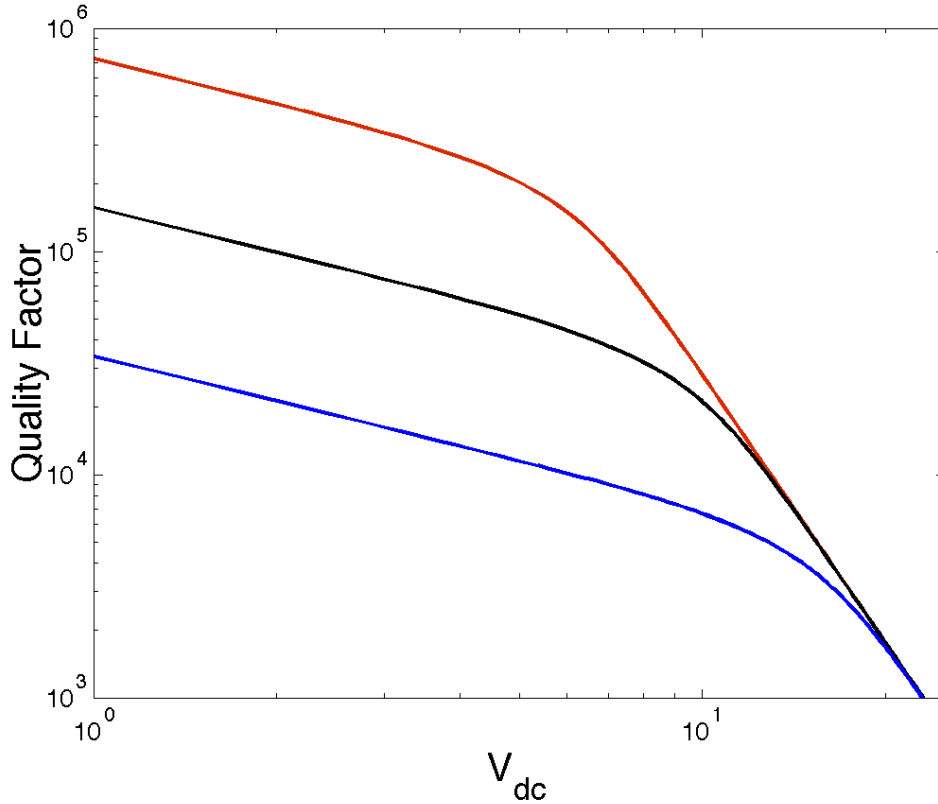


FIGURE 3.2: The quality factor  $Q$  as a function of bias voltage  $V_{\text{dc}}$ . The quality factor is evaluated for  $V_{\text{ac}} = 10 \mu\text{V}$  (blue line),  $V_{\text{ac}} = 100 \mu\text{V}$  (black line) and  $V_{\text{ac}} = 1 \text{ mV}$  (green line).

This analysis enables the calculation of  $\eta$ ,  $\gamma$  and  $Q$ . In the following, a graphene beam of suspended length  $1 \mu\text{m}$  and initial tension  $T_0 = 0.34 \text{ N/m}$  on top of a  $\text{SiO}_2$  substrate is considered. The coupling parameter  $\Lambda$  is taken from the literature to be  $\Lambda = 10^{20} \text{ N/m}^3$  [65], and the distance to the back-gate is  $d = 330 \text{ nm}$ . Furthermore, the total length of the graphene sheet is taken to be  $3 \mu\text{m}$ . For this particular geometry, the values  $\tilde{\eta} = 0.19$  and  $\delta = 0.42$  are obtained. Thus, nonlinear damping is not strong enough to obliterate the Duffing bistability. In fact,  $\tilde{\eta} < \sqrt{3}$  in all conducted simulations.

In figure 3.2, the quality factor  $Q$  is plotted as a function of  $V_{\text{dc}}$  for three values of the driving voltage  $V_{\text{ac}}$  at the vibrational resonance of the graphene resonator. There is a clear kink in the quality factor, signifying the transition from nonlinear to linear damping dominated regimes. The dependence of the quality factor on the bias voltage is

qualitatively different in the two regimes, something that could be used for experimental verification of nonlinear damping. Another signifying feature of the nonlinear damping regime is that the quality factor in this regime depends on the alternating voltage, while it is independent of alternating voltage in the linear regime.

For this particular geometry, the nonlinear damping will dominate for bias voltages  $V_{\text{dc}} \lesssim 10$  V. The resulting quality factor lies in the range  $10^4$ - $10^6$ , similar in magnitude to those reported in experiments of  $Q \sim 10^5$  [66]. The coupling between the flexural motion of the graphene sheet and the in-plane motion is therefore a contributing mechanism for dissipation, and should give rise to measurable nonlinear dissipation for small bias voltages. However, this mechanism alone will not remove the Duffing bistability.

### 3.3 Thermalization of nanoscale resonators

In the last section, I showed how the nonlinearity of graphene resonators affects the dissipation of the motion of the fundamental mode oscillations when it is coupled to an external medium. The nonlinear coupling between the out-of-plane and in-plane motions caused an amplitude dependent, nonlinear, dissipation. In this chapter the possibility of using the other oscillation modes of the graphene sheet as the heat bath is considered. This would imply that, even without any coupling to external heat baths, the energy of the fundamental mode would be distributed among all modes. This would set a lower limit on the dissipation of graphene resonators, and is therefore of key importance for applications. Since the form of the nonlinearity is determined solely by the geometry of the resonator, this lower dissipation limit is also set by the geometry. As in previous chapters, the drum and beam geometry are explicitly considered here.

Further, as repeatedly mentioned in this thesis, the question of energy relaxation in closed Hamiltonian systems touches upon fundamental questions in statistical physics in mesoscopic systems. Due to the strong nonlinearity in graphene resonators, I propose to use these as test beds for the large amount of theoretical results in this field.

The question regarding energy redistribution among modes in NEMS resonators consequently need to be addressed from two different viewpoints. The first question is: can the approach toward a thermodynamic equilibrium in these system help us gain further insight into statistical mechanics and Hamiltonian dynamics in finite sized systems? The second issue concerns the feasibility of using NEMS-systems for this purpose; in particular, is it possible to somehow distinguish the inter-mode relaxation processes from coupling to external heat baths?

For linear systems, the oscillation modes are uncoupled, and so the motion of mode  $n$  is not influenced by the motion of mode  $m$ . This is no longer true for nonlinear oscillators, where different modes are coupled. As was shown in chapter 2, the equations of motion for the modes of a generic, unbiased graphene resonator are on the form

$$\ddot{q}_n + \omega_n^2 q_n + \sum_{ijk} W_{ijkn} q_i q_j q_k = 0 \quad (3.17)$$

where the coupling matrix  $W_{ijkn}$  is determined by the geometry of the resonator. The Hamiltonian in the conjugate mode coordinates  $(p, q)$  will similarly be

$$H_g = \frac{1}{2} \sum_n (p_n^2 + \omega_n^2 q_n^2) + \frac{1}{4} \sum_{ijkn} W_{ijkn} q_i q_j q_k q_n \quad (3.18)$$

Singling out the fundamental mode, the Hamiltonian can be written

$$\begin{aligned} H_g &= \frac{1}{2} (p_0^2 + \omega_0^2 q_0^2) + \frac{1}{4} W_{0000} q_0^4 \\ &\quad + \frac{1}{2} \sum_{n \neq 0} (p_n^2 + \omega_n^2 q_n^2) + \frac{1}{4} \sum_{(ijkn) \neq 0} W_{ijkn} q_i q_j q_k q_n \\ &\quad + \frac{q_0}{4} \sum'_{(ijk) \neq 0} W_{ijk0} q_i q_j q_k + \frac{q_0^2}{4} \sum'_{(ij) \neq 0} W_{ij00} q_i q_j + \frac{q_0^3}{4} \sum'_{i \neq 0} W_{i000} q_i, \end{aligned} \quad (3.19)$$

where the prime on the sums implies that the sum is to be taken over all permutations of the indices. This gives a natural subdivision of the Hamiltonian into a system Hamiltonian, a bath Hamiltonian and a coupling Hamiltonian,

$$\begin{aligned} H_{\text{sys}} &= \frac{1}{2} (p_0^2 + \omega_0^2 q_0^2) + \frac{1}{4} W_{0000} q_0^4, \\ H_{\text{bath}} &= \frac{1}{2} \sum_{n \neq 0} (p_n^2 + \omega_n^2 q_n^2) + \frac{1}{4} \sum_{(ijkn) \neq 0} W_{ijkn} q_i q_j q_k q_n, \\ H_{\text{coup}} &= \frac{q_0}{4} \sum'_{(ijk) \neq 0} W_{ijk0} q_i q_j q_k + \frac{q_0^2}{4} \sum'_{(ij) \neq 0} W_{ij00} q_i q_j + \frac{q_0^3}{4} \sum'_{i \neq 0} W_{i000} q_i. \end{aligned} \quad (3.20)$$

There are some key differences between this Hamiltonian system, and the system considered in the previous section. First, the coupling in the previous chapter was quadratic in the mode amplitude, while here also a cubic coupling appears. Second, in the previous chapter the bath was a linear system, while here it is nonlinear, which makes the coupling terms nonlinear in the bath modes. Third, upon going to the rotating frame, the previous chapter showed that the energy transfer between the subsystem was dominated by the response of the bath at the fundamental mode frequency. Since the bath spectrum in the present case is discrete, it is not clear that the bath will have

a frequency response at the fundamental mode frequency at all, and therefore energy sharing between the modes may not be present. The dynamics of this kind of system is determined by the linear frequency spectrum and the coupling matrix. In a simplified picture, the linear spectrum contains information about which couplings remains upon going to the rotating frame, and consequently which couplings allow for energy transfer.

As a simple model system, one may consider the beam equation in the out-of-plane approximation,

$$\ddot{w} = \partial_x [(1 + w_x^2) w_x] \quad (3.21)$$

As it turns out, this is exactly the continuum limit of the FPU- $\beta$  problem, one of the best studied nonlinear systems around. Although adding the in-plane deformations to the model will change the dynamics, this similarity to the FPU problem suggests that some results may be directly transferred to the dynamics of graphene resonators. In particular three aspects of the problem are considered; namely the nature of the metastable state, the scaling of the equilibration time with energy and the scaling of the largest Lyapunov exponent with energy. It should be noted, that while one in the FPU literature makes a distinction between total energy of the system and "specific" energy, i.e. the energy per mode or equivalently the energy per oscillator, this distinction is meaningless in the continuum limit and makes sense only when the equations of motion are projected onto mode space. By energy I will always mean energy density, or specific energy, unless otherwise stated.

### 3.4 Internal relaxation in nanobeams

First, consider a graphene nanobeam. As mentioned previously, the beam equation in the out-of-plane approximation is identical to the continuum limit of the FPU- $\beta$  problem. The situation changes when the in-plane deformation field is taken into account. The equations of motion are then

$$\begin{aligned} \partial_x(2u_x + w_x^2) &= 0, \\ \ddot{w} &= w_x x + \partial_x [(2u_x + w_x^2) w_x]. \end{aligned} \quad (3.22)$$

As is shown in appendix A, the coupled mode equation for this system can be written as

$$\ddot{q}_n + \left( \omega_n^2 + \sum_m \omega_m^2 q_m^2 \right) q_n = 0, \quad (3.23)$$

which means that the frequencies of the modes are renormalized by the presence of other modes. As was argued in the previous section, significant energy sharing among modes require the development of chaos in the system. This in turn implies a loss of stability of some, or all, fixed points of the system. The fixed point in question is clearly  $q_n^* = 0$ ; if this fixed point ceases to be stable, mode  $n$  will be excited due to the motion of the fundamental mode. If, initially, only one mode is excited, the equation above is essentially the Mathieu equation,

$$\ddot{q}_n + (\omega_n^2 + \omega_0^2 \tilde{q}_0^2 \cos^2(\omega_0 t)) q_n = 0 \quad (3.24)$$

where  $\tilde{q}_0^2$  is the amplitude of the single mode excitation and  $\omega_0$  its frequency. This equation will be unstable for  $\omega_n^2 + \frac{\omega_0^2 \tilde{q}_0^2}{2} < 0$  and for  $\omega_0 \approx \omega_n$ . Since  $\omega_n^2 + \frac{\omega_0^2 \tilde{q}_0^2}{2}$  cannot be smaller than zero, instability will occur only for  $\omega_0 \approx \omega_n$ , so called parametric excitation. However, since the spectrum is discrete,  $\omega_0$  and  $\omega_n$  will always be well separated. From this, we conclude that chaos, and consequently significant energy sharing among modes, will not be present for the one-dimensional beam as long as the system can be characterized by well defined mode frequencies. Nonetheless, (3.23) suggests that the coupling between modes causes fluctuations of the frequency of the modes. Consequently, the lineshape will be broadened by these fluctuations. This spectral broadening is not related to dissipation of energy, but rather to dephasing. This type of broadening has been observed experimentally [67], which gives additional support for the possibility of directly observing the mode coupled dynamics in graphene resonators.

It should be noted that taking the full two dimensional model of the beam, including the bending rigidity of the beam, or introducing defects in the beam will break the symmetry of the equations and allow for energy sharing. Following the same line of reasoning, a carbon nanotube may be expected to display some energy relaxation due to the relatively large bending rigidity. However, these models would be treated as perturbations to the non-chaotic model and so the relaxation can be expected to be rather slow, possibly undetectable experimentally. The other route to observing energy relaxation would be to change the form of the nonlinearity, or in other words to change the geometry.

### 3.5 Drum geometry

The drum geometry is a nontrivial extension of the original FPU problem. As noted in chapter 2, the coupling matrix  $W_{ij;kl}$  is dense, with permutation symmetry in the indices  $i \leftrightarrow j$  and  $k \leftrightarrow l$ . This implies that no simple selection rules for the indices as was the case for the FPU chain will exist in this case.

The relaxation and thermalization process for the drum geometry has additionally been investigated using molecular dynamics simulations (MD) performed at Boston University. The two models complement each other: the theory underlying the MD equations is atomistic and more fundamental than the field theoretical approach taken in this thesis. At the same time, the MD simulations are much more computationally heavy than a straightforward numerical integration of the coupled mode equations (3.17). Further, the continuum mechanics model is parameter free, and the results can therefore be directly scaled to any physical realization of the drum resonator, while the MD simulations are performed for specific sets of system parameters. Consequently, the MD simulations are used to obtain quantitative results on the thermalization process for small system sizes and short times. The results of the MD simulations are compared to the results from a numerical integration of the coupled mode equations.

It is not a priori clear that the two models should give consistent quantitative results in any physical limit. The reason is twofold: firstly, the MD simulations contain dynamics on length scales that are comparable to the bond length in the graphene sheet. These high frequency fluctuations cannot be handled in a continuum model. Further, the mode coupling model employed here only takes radially symmetric modes into account. The angular modes may give rise to additional relaxation channels in the system.

If the high frequency fluctuations couple only weakly to the fundamental mode, the two models should at least qualitatively agree already for a small number of considered modes in the continuum model. This is consistent with the so called Boltzmann-Jeans conjecture of freezing of high-frequency degrees of freedom. Such freezing phenomena are well known to occur in nature, the best known example possibly being the specific heat of diatomic gases. Diatomic gas molecules have seven degrees of freedom; three corresponding to translations, two to rotations, and two internal degrees of freedom due to vibrations. Consequently, classical statistical mechanics predicts a specific heat of  $7/2R$ , while experimentally one has  $3/2R$  at sufficiently low temperatures, with  $R$  being the universal gas constant. It therefore seems as though only the translational degrees of freedom contributes to the specific heat; the rotational and vibrational degrees of freedom appears to be frozen.

To convince oneself that the truncated coupled mode equations can be used to study the fundamental mode dynamics of a circular graphene sheet, one needs to show that the highest mode only weakly couples to the fundamental mode. To this end, I consider a system of 32 modes, with initially all energy in a high frequency mode (for specificity I have chosen the 16th). Then, the energies of the individual modes are monitored for a time large compared to the frequency of the fundamental mode. The evolution of the mode energies is shown in figure 3.3. The system quickly approaches a quasi-equilibrium

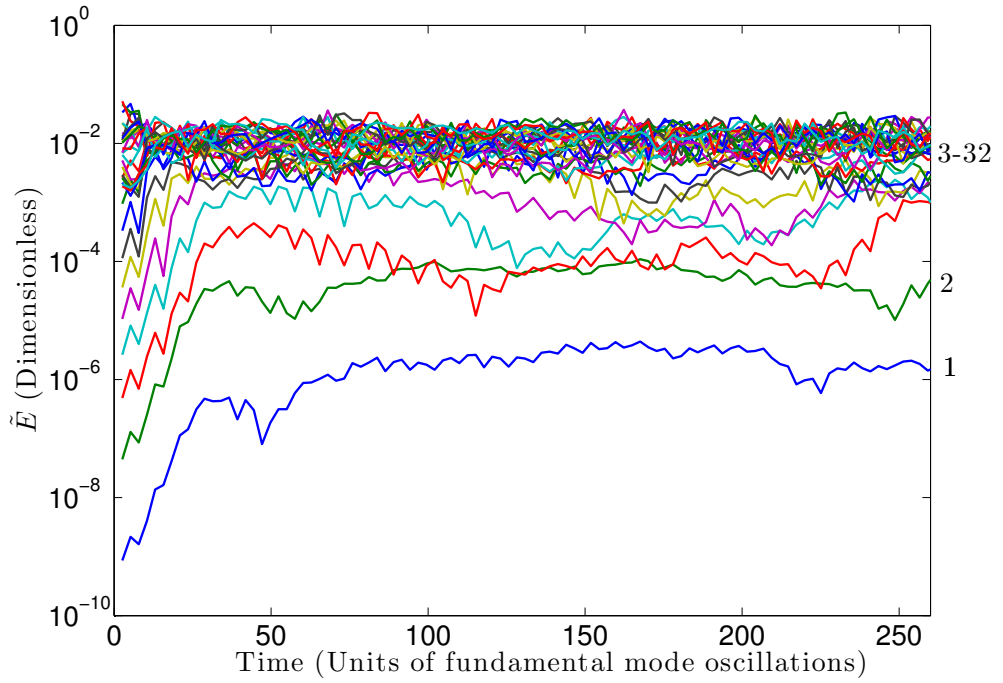


FIGURE 3.3: Time evolution of the modal energies evaluated from the continuum theory, when initially all energies in the 16th mode. Mode numbers are indicated on the right. The higher modes equilibrate quickly, while the lowest modes are essentially decoupled from the dynamics.

situation where a subset of the modes share the energy, but the low frequency modes are essentially disconnected from the dynamics. This implies that already 32 modes are sufficient to separate the dynamics into a "bath", consisting of the high frequency modes, and a "system" of low frequency modes, with only weak coupling between system and bath, but strong mixing and fast relaxation within the bath. For more traditional FPU-type initial conditions, with all energy in the fundamental mode, the metastable state significant for the FPU problem is recovered. The system evolves non-chaotically for a long time  $\tau_m$ , and then undergoes relaxation toward equipartition during a time  $\tau_{tr}$ . This is exemplified in figure 3.4 a), where the energy of the fundamental mode normalized to the total energy of the system is reported. A normalized energy of 1 means that all energy is concentrated to the fundamental mode, or equivalently that the bath is kept at  $T = 0$  K. As energy is fed from the fundamental mode to the bath modes, the temperature of the bath increases accordingly, and so the normalized energy decreases.

In figure 3.4 a), several simulations of the coupled mode equations have been performed at a fixed total energy but with different distributions of energy among the modes. An effective bath temperature is simulated by drawing initial conditions for the bath modes from a Boltzmann distribution. The remaining energy is then fed to the fundamental mode. In other words, the system energy is fixed but the initial ratio of fundamental

mode energy to total energy varies. By shifting the time for the different simulations, so that at time  $t = 0$  the ratio between fundamental mode energy and total energy is  $1/2$ , the evolution of the fundamental mode energies align. This implies that as energy is fed from the fundamental mode to the higher modes, the higher modes thermalize on a faster time scale and is always in a thermal equilibrium. Consequently, the evolution of the fundamental mode will follow a universal curve given by the fitted sigmoid function in the figure. Changing temperature and initial excitation of the fundamental mode while keeping the total energy fixed will simply constitute a shift in time along this curve.

This implies that the metastable state is very sensitive to temperature; increasing the temperature from  $T = 0$  K very quickly gives a dramatic shift in time along the universal evolution curve, and the system enters the violent relaxation phase. As a result, the metastable state is probably difficult to observe experimentally.

The violent relaxation phase is then more promising for experimental observation. This phase has been studied both using the coupled mode equations and using MD simulations. For the coupled mode equations the time scale for the violent relaxation was extracted by fitting the dynamics to sigmoid functions as in figure 3.4 a). As the MD simulations are much more computationally expensive, the time scale was extracted by considering the maximal relaxation rate during the thermalization process. From figure 3.4 a) it is clear that this occurs when the ratio of fundamental to total energy is roughly  $1/2$ . Consequently, for the MD simulations the initial configuration was chosen so that the ratio was initially close to this value.

Since, as argued above, changing the temperature and initial excitation velocity independently would in general change both the total energy and the ratio of fundamental to total energy, a peculiarity of the scaling of the dimensionless energy was used to change the total energy without changing the ratio. In terms of temperature, the dimensionless energy can be written as

$$\tilde{E} = \frac{1}{2\epsilon^2} \frac{\kappa}{m_c c_L^2} \quad (3.25)$$

where  $m_c$  is the mass of a carbon atom,  $\epsilon$  is the pre-strain of the system and  $\kappa$  is the average energy per atom. In thermodynamic equilibrium,  $\kappa = k_B T$ . Out of equilibrium, one may define an effective temperature by considering the energy not residing in the fundamental mode,  $k_B T^* \equiv (E - E_0)/N$ , where  $E$  is the total system energy,  $E_0$  is the fundamental mode energy and  $N$  is the number of degrees of freedom. The relation (3.25) shows the correspondence between temperature and strain in this system. The importance of the mode coupling is determined by the thermal fluctuations of the membrane. These may be enhanced either by increasing the temperature, or by decreasing the strain. To vary the total dimensionless energy of the graphene without changing the

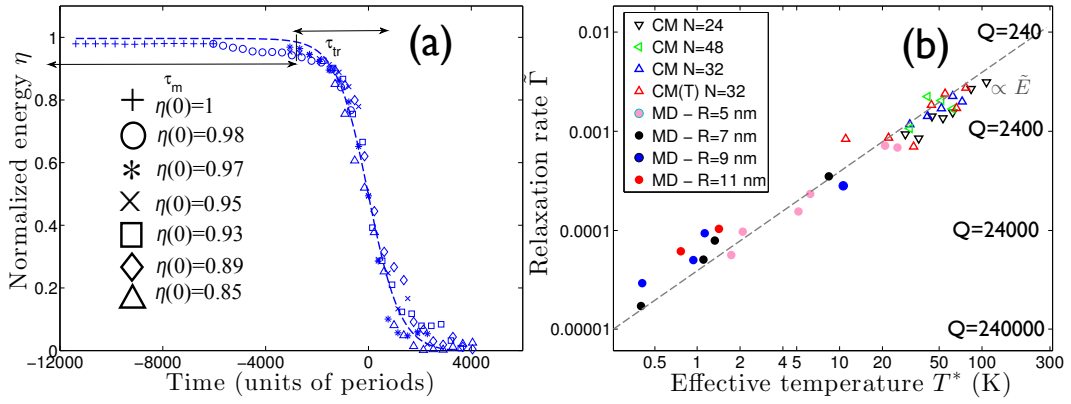


FIGURE 3.4: a: Simulation of mode coupled equations for a fixed total energy, but with varying initial energy in fundamental mode. By shifting time, the curves align. The solid line is a fitted sigmoid function used to extract the transition time  $\tau_{tr}$ . b: Extracted rates  $\Gamma = \tau_{tr}^{-1}$  from MD simulations (filled symbols) and continuum mechanics (open symbols). The dashed line corresponds to a linear scaling with dimensionless energy.

initial ratio of fundamental to total energy, both temperature and velocity were kept fixed while the strain  $\epsilon$  was changed.

The resulting scaling of the relaxation rate with dimensionless energy is reported in figure 3.4 b). The scaling is linear for the considered energies. Further, there is no dependence on the dimensionless relaxation rate on the size of the drum. This is consistent with the observation that the dimensionless energy in (3.25) does not contain any length scale.

These results also give a hint on how the mode coupling and thermalization in graphene resonators may be experimentally detected. First of all, the mode coupling mechanism implies a *size independent* relaxation. This is in contrast to what has previously been reported for drum resonators by the Cornell group, where a power law dependence on drum radius was observed [68]. However, the graphene resonators they considered were CVD grown. It is known that CVD grown graphene suffer from grain boundaries. The size of the grains then introduces an additional length scale into the problem, which makes the continuum mechanics model employed here invalid unless the resonator is very large compared to the grain sizes.

Secondly, the relaxation is set by the dimensionless energy of the graphene. The temperature and the strain enters into the scaling as  $T/\epsilon^2$ , which implies a relation between the temperature scaling of the relaxation and the scaling with strain.

Finally, a potential problem for experimentally observing ring-down in circular graphene resonators is noted. The frequency of the fundamental mode is observed to decrease during the ring-down, due to the decrease in energy of that mode. The decrease is observed both in MD simulations and continuum mechanical simulations, and the results

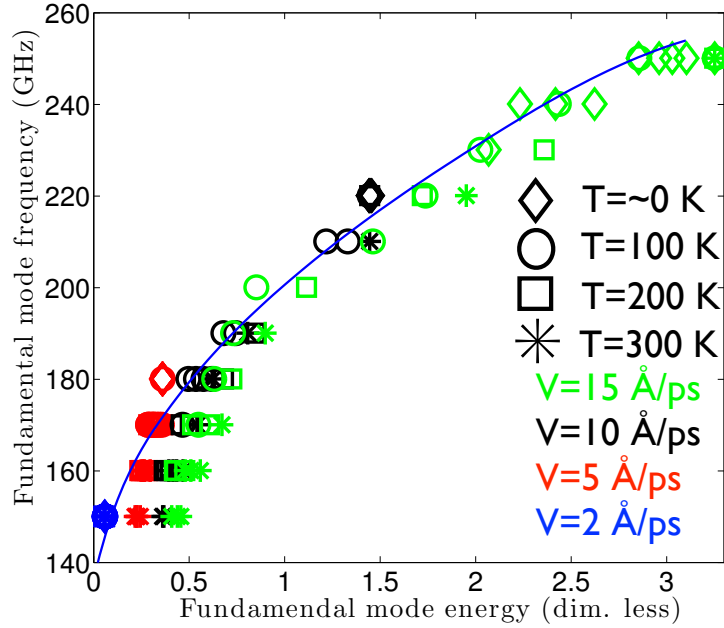


FIGURE 3.5: Fundamental mode frequency as a function of mode energy. Symbols correspond to molecular dynamics results, while the full line is the curve predicted from continuum mechanics.

agree quantitatively as is shown in figure 3.5. This decrease in frequency poses a problem experimentally, since it may not be possible to observe ring-down by locking in to a specific frequency.

As the scientific community has gathered results on the FPU-chain in its traditional form for over five decades, the present study is by no means exhaustive regarding the thermalization and equilibration properties of graphene nano drums. It is merely intended as a proof of concept, suggesting the use of graphene nano drums as physical test beds for nonlinear non equilibrium systems. In particular, the existence of a strong stochasticity threshold as reported in the FPU chain would be a logical next step in the theoretical investigation of the model. If such a threshold exist at physically reasonable energies, this could also be used for experimental verification and observation of the coupled mode dynamics.

## Chapter 4

# Bending rigidity of graphene

In all previous models in this thesis, the energy cost of bending the graphene sheet has been disregarded. This is often a valid approximation, particularly when the sheet is under tension. At Gothenburg University, devices have been fabricated where *compressive* strain is used to engineer the shape of the suspended graphene sheet. The compressive strain is achieved through thermal cycling before making the graphene suspended. Upon suspending the graphene, the compressive strain is released and the graphene buckles. The interaction with the electrodes breaks the spatial symmetry of the buckling, causing the graphene to buckle toward the electrodes. This way, the graphene buckles can be assessed electrostatically (figure 4.1). In these prebuckled structures, the response to an applied pressure is determined by the relative balance between bending and stretching energy. As a consequence, the bending rigidity of the graphene can no longer be neglected. Since the bending rigidity has a very limited effect on the mechanical properties of graphene in most structures, the numerical value of this parameter is much less established than the elastic stiffness of graphene. In the present case, the response of the sheet will be determined by the relative balance of the elastic stiffness and bending rigidity. Hence, these structures give us a unique opportunity to measure the bending rigidity directly. Before describing the details of the measurements, I give a brief review on the current status of the bending rigidity of graphene.

### 4.1 Bending rigidity of graphene: current status

The bending rigidity of bulk elastic materials is due to the stretching and compression in different parts of the material as a consequence of the bending deformation. The bending rigidity of such materials scale with thickness and Young's modulus as  $\kappa \sim Eh^3$ . For monolayer graphene, this tension-compression model of bending stiffness does not apply,

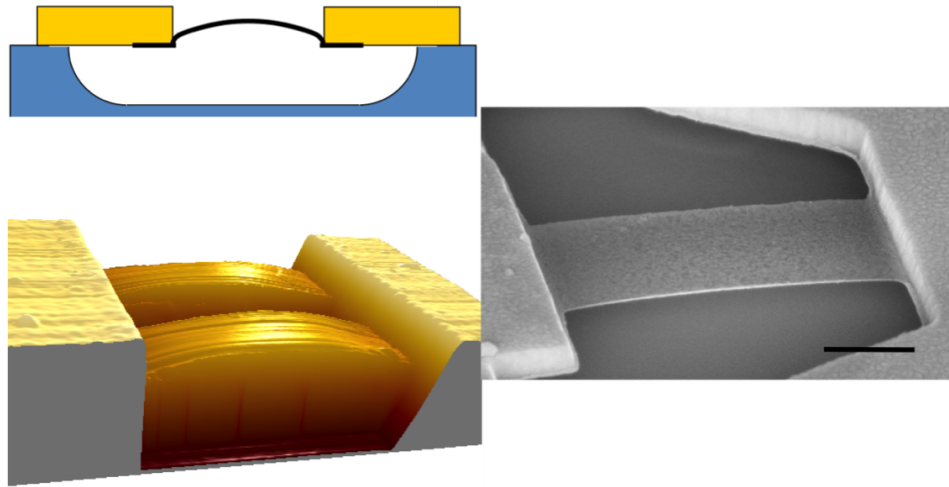


FIGURE 4.1: Visualisation of the buckled structures. The upper image is a schematic image of the resulting structure. Beneath it to the left is an AFM image of an experimental structure, and to the right an STM image. In both images the resulting curvature is clearly visible.

since graphene is two dimensional. The bending rigidity must therefore have a different origin.

One such origin is the change in bond angles in the hexagonal atomic structure associated with changing the curvature of the graphene sheet. This effect can be estimated using so called bond order potentials, an empirical set of potentials designed to describe the energetics of molecular bonds. Estimates based on bond order potentials as well as *ab initio* calculations give values of  $\kappa \sim 1$  eV [69–71].

It is worth noting that this estimate is given in the limit of zero temperature. At higher temperatures, thermal fluctuations causes ripples in the graphene sheet that are approximately 80 Å wide and that screen long wavelength deformations such as bending. The bending rigidity is consequently increased to about  $\sim 2$  eV at  $T = 3500$  K [72].

Admittedly, this predicted increase in bending rigidity by a factor of two when increasing the temperature from 0 K to 3500 K does not imply a dramatic thermal effect. The case is quite different, in fact, when moving from a single graphene layer to a bilayer [73]. At low temperatures the two layers follow each other rigidly, reinstating the tension-compression model as the primary origin of bending stiffness already for membranes only two atoms thick. The bending rigidity here is easily estimated considering two thin plates separated by a distance  $h$ . When deforming this system, we consider a hypothetical neutral surface between the thin plates that is not stretched. If the system

is bent into a cylinder with radius of curvature  $R$  at the neutral surface, the radii of curvatures of the two plates become  $R + h/2$  and  $R - h/2$  respectively. Compared to the nonstretched neutral surface, the relative tension/compression of an infinitesimal length element on each of the plates is consequently given by  $h/2R$ . The energy associated with this deformation is  $\Delta E = \frac{T_1}{2} \left(\frac{h}{2R}\right)^2$  for each plate, where  $T_1 = \lambda + 2\mu$ . The bending rigidity is the parameter in the free energy multiplying the inverse radius of curvature squared. Thus,  $\kappa = T_1 \frac{h^2}{4}$ . Using  $T_1 = 340$  N/m [74] and  $h = 3.4$  Å, this evaluates to  $\kappa \sim 160$  eV. This naive estimate is in excellent agreement with *ab initio* calculations using bond order potentials, giving values ranging from 160 to 180 eV [70] at  $T = 0$  K. Thus, the energy of bending a bilayered graphene sheet at low temperatures mainly comes from the tension-compression energy, indicating that elasticity theory again prevails.

If, however, the temperature is increased from  $T = 0$  K, the individual graphene layers will create the same kind of thermal ripples as described above. At short distances, the graphene layers will appear to move independently, meaning that the bending rigidity on this length scale ( $\sim 80$  Å) is drastically reduced to that of two monolayer graphene sheets, i.e. 2 – 4 eV. At the same time, the graphene sheets appear to conserve stacking order despite the rippling. On longer length scales the sheets therefore do not move independently, and a significantly larger bending rigidity is expected. Thus, the issue of bending rigidity of bilayered graphene on experimentally relevant length scales is far more involved than its monolayered counterpart and experimental determination of this parameter, both for monolayered and few-layered graphene, is of significant importance for our understanding of the microscopic behavior of graphene.

## 4.2 Measuring the bending rigidity

As mentioned previously, the energy cost of bending a graphene sheet is extremely small compared to the energy required to stretch the sheet, so small that the former is typically neglected completely compared to the latter when modeling the mechanics of flat suspended graphene. It is therefore very difficult to experimentally estimate the value of this parameter by directly investigating the mechanical response of the graphene. In fact, prior to our work the only reported experimental estimate of the bending rigidity of monolayered graphene comes from studies of the phonon spectrum of graphite [75], giving values consistent with *ab initio* calculations. On the other hand, nano-indentation measurements have proven successful for determining the bending rigidity of thicker flakes (more than 8 layers) [76] where the difference in energy scales between bending and stretching is less pronounced.

In the measurement scheme developed by our group in collaboration with an experimental group at Gothenburg University, the inherent difficulties in measuring the bending rigidity are avoided by tuning the geometry to our advantage. Through thermal cycling a compressive strain is built up within the graphene sheet, which is released when the sheet is suspended causing the sheet to buckle (figure 4.2). When an external pressure is applied to these prebuckled structures, the resulting deformation is small until a critical pressure is reached, where the structures display a snap-through instability. This instability is probed by gradually increasing the voltage on the back gate while keeping an AFM tip in tapping mode on the graphene structure. The sudden change in height on the AFM is a signature of the snap through. A typical structure with snap through instability is shown in figure 4.2. A schematic image of the process of snap-through is seen in figure C.1.

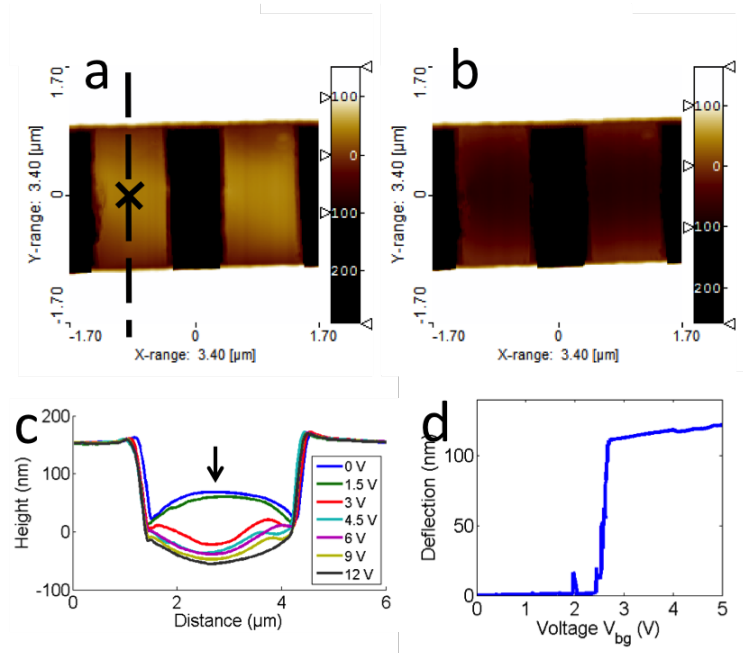


FIGURE 4.2: A doubly clamped structure showing a snap through instability. a) and b) are AFM images of the sample at 0 V and 3 V, respectively. In c), AFM sweeps have been made along the dashed line in a) while gradually increasing the voltage. In d) the AFM tip is kept fixed at the spot marked with a cross in a) while gradually increasing the voltage. Here, the snap-through instability manifests itself as the discontinuity in tip position at 2.6 V.

The instability was observed also in fully clamped structures, depicted in figure 4.3. For fully clamped structures, continuum elasticity theory gives an expression for the critical pressure [77],

$$p_c = \frac{4\sqrt{\kappa n T_1}}{R_1 R_2} \quad (4.1)$$

where  $n$  is the number of graphene layers and  $R_1$  and  $R_2$  are the principal radii of curvature. It is worth noting that the instability requires curvature in two directions, or,

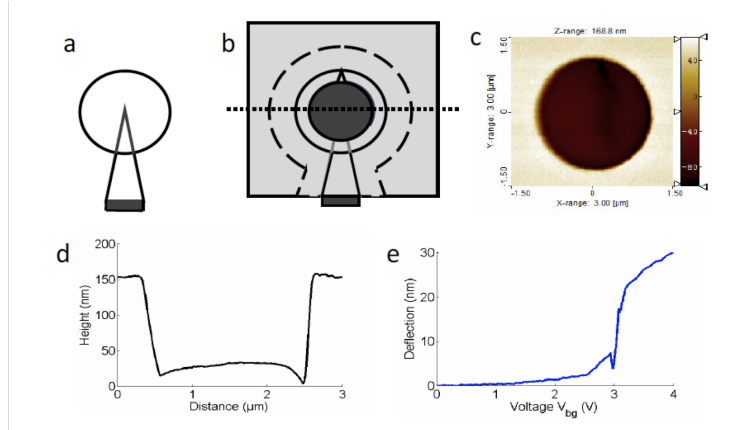


FIGURE 4.3: A fully clamped structure showing a snap through instability. a) and b) are AFM images of the sample at 0V and 3V, respectively. In c), AFM sweeps have been made along the dashed line in a) while gradually increasing the voltage. In d) the AFM tip is kept fixed at the spot marked with a cross in a) while gradually increasing the voltage. Here, the snap-through instability manifests itself as the discontinuity in tip position at 3V.

equivalently, a nonvanishing Gaussian curvature. This is due to a result from differential geometry, stating that pure bending can occur only in surfaces with a vanishing Gaussian curvature. Thus, to obtain the desired competition between bending and stretching, one needs curvature in two directions. Since the bending rigidity is very small for graphene membranes, a sheet with vanishing Gaussian curvature will respond easily to an applied pressure through pure bending. The detailed calculation leading up to equation (4.1) is far too involved to be included in this thesis; the reader is here referred to Pogorelov [77]. The scaling of the critical pressure can, however, be found from rather simple considerations (see appendix C).

Plotting  $V_{\text{cr}}^4$  versus  $R^{-4}$  on a logarithmic scale for the fully clamped structures, the experimental values are expected to fall along a straight line with unit slope. The bending rigidity can then be extracted from the intersection of the line with the  $y$ -axis. The experimentally obtained values for the fully clamped structures, all bilayers, are shown in figure 4.5. It is seen that the scaling is consistent with the one derived above. Using the analytical expression from Pogorelov, we were able to fit the bending rigidity, giving  $\kappa \approx 30_{-15}^{+20}$  eV. The rather large error bars here are mainly due to the smallness of the data set considered, and are not inherent to the method itself.

For the beam structures, the data points are expected to fall along a line with unit slope when plotting  $V_{\text{cr}}^4$  versus  $R^{-3}$ . Also the beam structures follow the expected scaling, as seen in figure 4.5. In this data set both bilayers and monolayers are present. Using the value of the bending rigidity extracted for the bilayers, we found a monolayer bending rigidity of  $\kappa \sim 7_{-3}^{+4}$  eV. Again, the error bars are large mainly due to the very small data set (only two monolayered structures were successfully fabricated and measured).

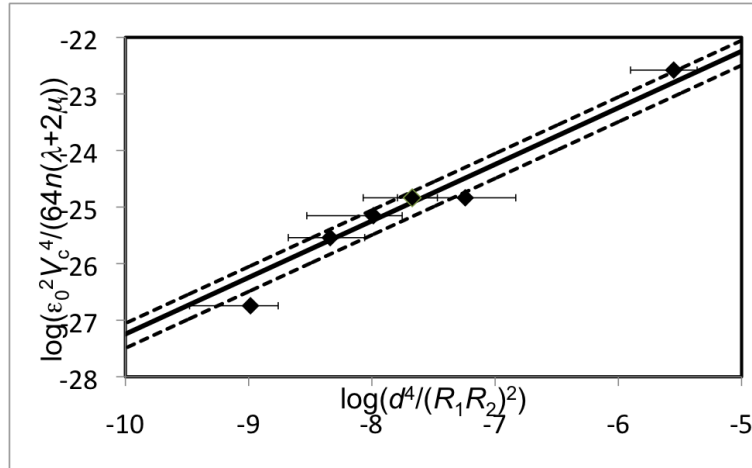


FIGURE 4.4: Scaling of the snap-through voltage with radius of curvature for fully clamped bilayer drums. The full line is a least squares fit, while the dashed lines represent the uncertainty. The scaling is consistent with theoretical considerations.

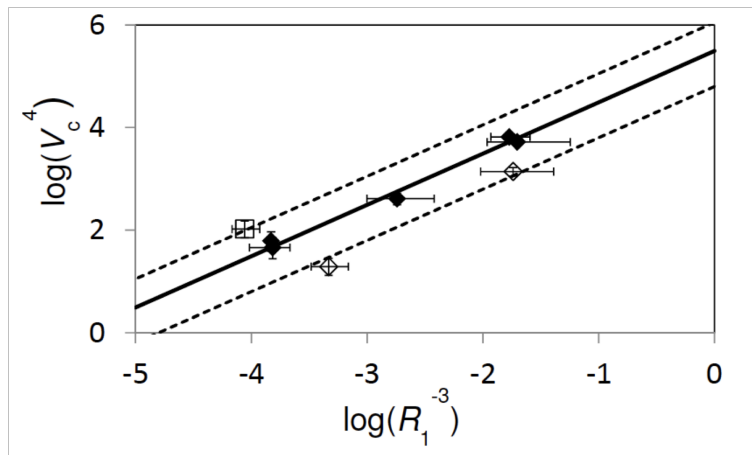


FIGURE 4.5: Scaling of the snap-through voltage with radius of curvature for doubly clamped beams. The open diamonds are monolayers, full diamonds bilayers and open square trilayer. The scaling is consistent with theoretical considerations.

## Chapter 5

# Parametric excitation of carbon nanotube single electron transistors

In the previous chapters, the focus has been entirely on the nonlinear properties of nanomechanical resonators, and the electromechanical actuation scheme was introduced only as necessary a means to induce the mechanical motion of the resonators. However, the coupling between electronic and mechanical properties is important in its own merit. First of all, most anticipated applications of NEMS devices employ electric readout. Secondly, coupling mechanical motion to additional degrees of freedom introduces new physics that is interesting in its own right.

In systems studied independently by the group of Bachtold in Barcelona and van der Zant in Delft [78, 79], the coupling between the mechanical motion of the resonator and the electronic quantum state of the electrical system is particularly strong. In fact, the addition or subtraction of a single electron to the resonator changes its mechanical properties in a measurable way.

The structure at hand is schematically depicted in figure 5.1. A doubly clamped carbon nanotube (CNT) is coupled via tunnel barriers to two electrodes, referred to as source and drain. The current between source and drain is modified by mechanical vibrations of the nanotube, typically induced by applying an oscillating voltage to the tube via the gate electrode, situated beneath the tube.

As was described in chapter 2, the presence of a significant bending rigidity in CNTs introduces a linear term in the equations of motion that is not present for graphene

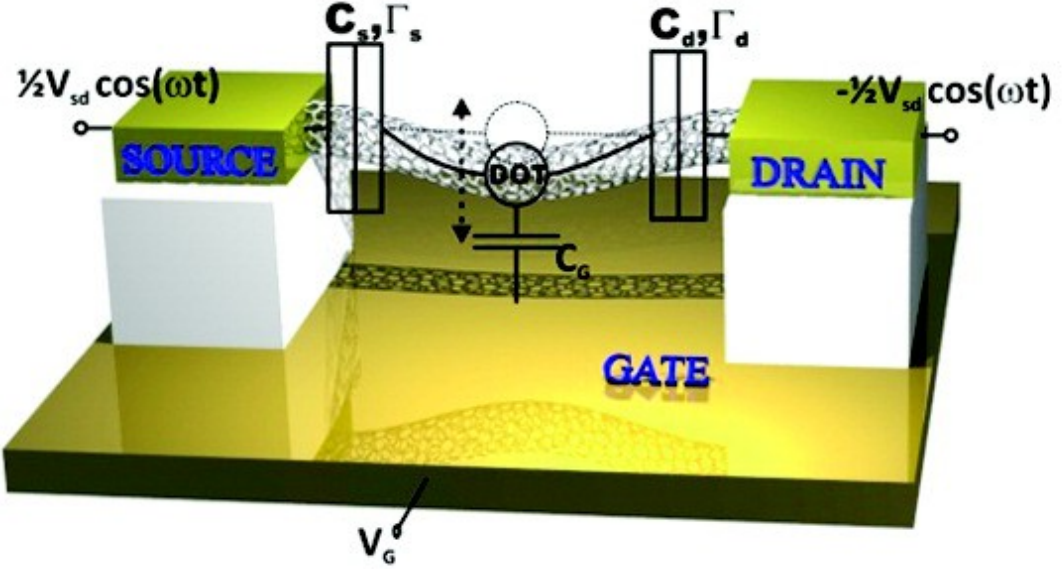


FIGURE 5.1: Visualization of the considered structure. A carbon nanotube with a quantum dot residing on it is coupled via tunneling barriers to two electrodes, source and drain. Beneath the tube there is a gate electrode capable of shifting the chemical potential of the quantum dot. Image provided by Yury Tarakanov.

resonators. I therefore disregard the mechanical nonlinearities and consider only the nonlinearities induced by the electromechanical coupling.

The electrical properties of the CNT is described as those of a *quantum dot*. A quantum dot is a small (essentially zero-dimensional) structure in which the electronic wave functions are confined in all spatial directions. In practice, this means that the energy quantization of the electronic levels is directly observable. The level spacing will be due partly to the quantization of the electronic wavelengths in spatial confinement, and partly due to an effect known as *Coulomb blockade*. If an additional electron is to enter the dot, it must first overcome the electrostatic potential from the electrons already residing on the dot: this will lead to an energy gap between the occupied and empty states on the dot. This energy gap is called the charging energy of the dot and is given by

$$E_{\text{ch}} = \frac{e^2}{C_{\text{dot}}}, \quad (5.1)$$

where  $C_{\text{dot}}$  is the capacitance of the dot. [80]

If the thermal energy is small compared to this charging energy, changes in the electronic occupation of the dot can be experimentally observed. A quantum dot connected as shown in figure 5.1 is called a single electron transistor (SET). The tunneling probability



The groups in Barcelona and Delft found that the resonance frequency and damping of the mechanical motion of the nanotube changes significantly when the average electron occupation on the dot changes. This can intuitively be understood by considering the equation of motion for the fundamental mode oscillation of the tube,

$$\ddot{q} + \gamma\dot{q} + \omega_0^2 q = F_{\text{cap}} + F_{\text{dot}} \quad (5.2)$$

where  $F_{\text{cap}}$  is the ordinary electrostatic force due to capacitive coupling considered in chapter 2, and  $F_{\text{dot}}$  is the contribution to the force from the single electron tunneling effect. This additional force will be proportional to the occupation of the dot. The occupation changes abruptly whenever the chemical potential of the dot aligns with the chemical potential of the leads. The chemical potential of the dot is given in terms of the tube deflection by

$$\mu_{\text{dot}} = \mu_{\text{DC}} - \frac{dC_{\text{g}}}{dq} \frac{eV_0}{C_{\text{dot}}} q \quad (5.3)$$

where  $\frac{dC_{\text{g}}}{dq}$  is the derivative of the gate capacitance with respect to the deflection,  $V_0$  is a reference voltage and  $\mu_{\text{DC}}$  is the chemical potential in the absence of deflection. Consequently, the force will depend strongly on the tube deflection in the region where the dot occupation changes. The shift in spring constant, or equivalently in resonance frequency, is given analytically as a function of the chemical potentials by

$$\delta k = \frac{dF_{\text{dot}}}{dq} = \left( \frac{dC_{\text{g}}}{dq} V_0 \right)^2 \frac{1}{2C_{\text{dot}} k_{\text{B}} T} \left[ 1 + \frac{E_{\text{ch}}}{2} \left( f' \left( \frac{\mu_{\text{dot}} + \mu_{\text{sd}}}{k_{\text{B}} T} \right) + f' \left( \frac{\mu_{\text{dot}} - \mu_{\text{sd}}}{k_{\text{B}} T} \right) \right) \right] \quad (5.4)$$

where  $f(x) = \frac{1}{1+e^x}$  is the Fermi function. This is shown in figure 5.3 as a function of the dot chemical potential. As is seen, the spring constant shift is maximal when the argument of the Fermi function vanishes.

In the experiments in Barcelona and Delft, the actuation of the mechanical motion of the device is achieved by periodically modulating the back gate voltage. This introduces a force on the dot both from the capacitive term  $F_{\text{cap}}$  and through the single electron effect. However, to really study the strong coupling it would be desirable to have an actuation that only affects the nanotube through the single electron effect. It is clear that such a scheme cannot rely on the gate voltage since the gate voltage introduces a capacitive forcing. In paper V, I show that the desired actuation can be achieved through an oscillating source-drain voltage.

From figure 5.3, one infers that changing the source-drain voltage changes the shift in resonance frequency at the degeneracy point. Consequently, an oscillating source-drain voltage causes an oscillating frequency shift. Further, since the frequency shift is independent of the sign of the voltage, this shift is modulated at twice the oscillation

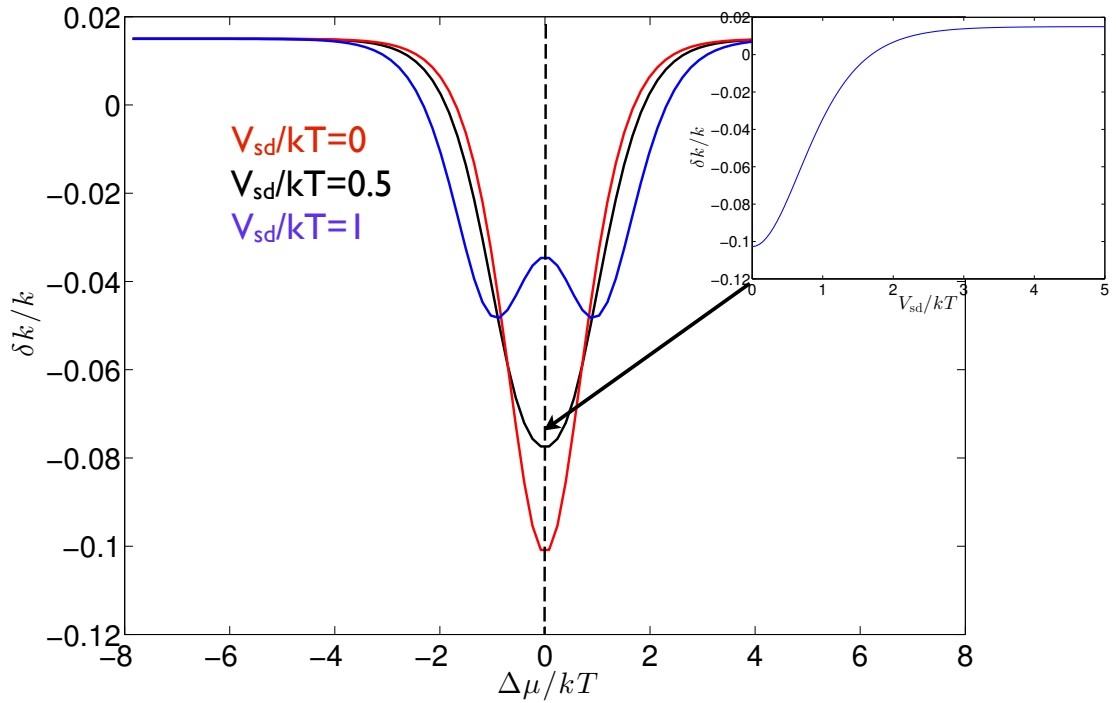


FIGURE 5.3: The resonance shift due to single electron tunneling as a function of the misalignment in chemical potentials of dot and lead at various source-drain voltages. The shift is strongly peaked at the degeneracy point, where the chemical potentials align. The inset shows the frequency shift at the degeneracy point as a function of source drain voltage. Applying an oscillating source-drain voltage causes an oscillatory frequency shift.

frequency of the source-drain voltage. It is well known that modulating the frequency of an oscillator at twice its fundamental frequency causes the system to undergo what is known as a parametric instability. The system will start to oscillate at the fundamental frequency. The instability is present in a narrow range of frequencies, the width of which is determined by the linear damping in the system. This implies that the mechanical motion displays a very strong sensitivity to the modulation frequency, which makes parametrically excited structures interesting for filtering applications. Further, the amplitude of these oscillations is not set by the linear damping but by nonlinearities in the system. Consequently, this kind of system could be used to study nonlinear effects in nanoresonators.

As a final note, the amplitude of the frequency modulation saturates if the source-drain voltage is too large. The parametric driving will then be weakened, which implies that the effect is present for a finite range of source-drain voltages and modulation frequencies. This is shown in figure 5.4, where the mechanical oscillation amplitude is shown as a function of modulation frequency and source-drain voltage. In the figure, the time evolution of the fundamental mode oscillations inside and outside the region of parametric excitation is additionally shown.

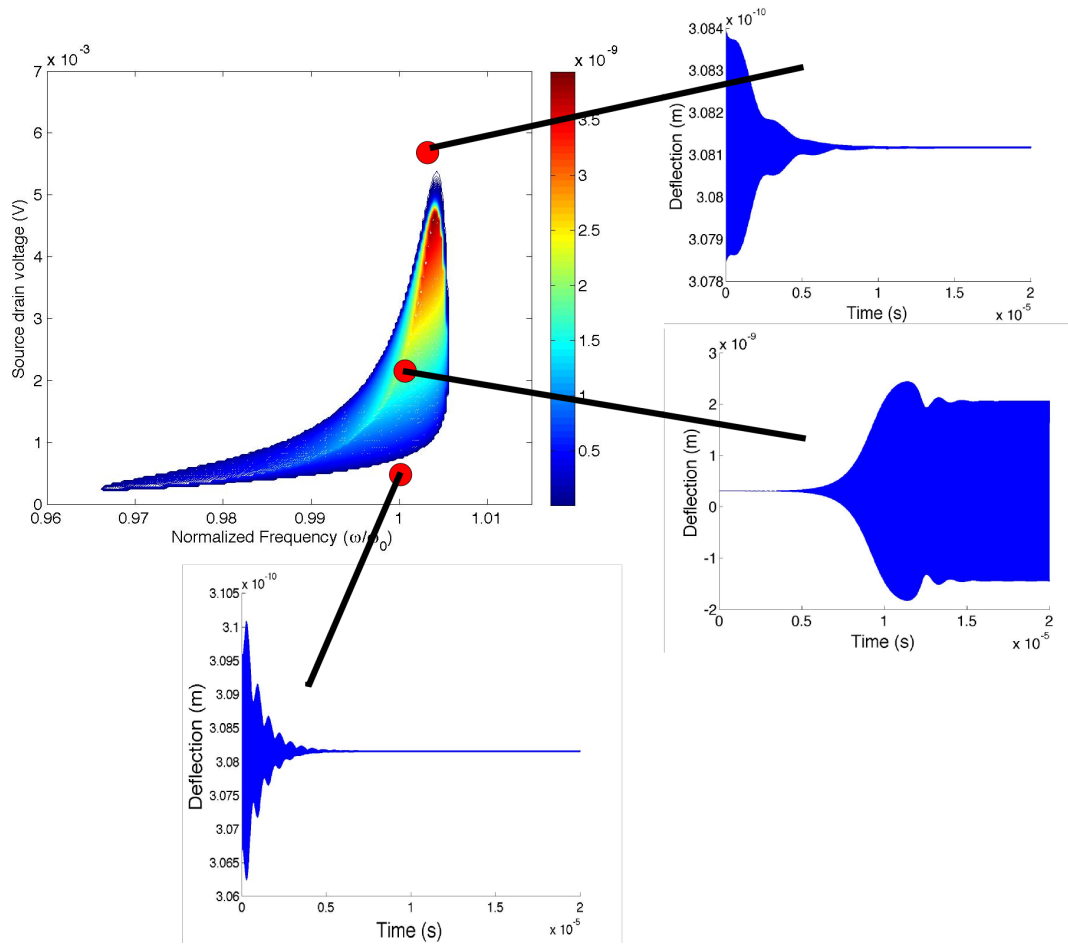


FIGURE 5.4: Contour plot of the deflection amplitude (in nanometers) at the modulation frequency  $\omega \approx \omega_1$  when the dot is biased at the degeneracy point. Note the boomerang shape of the region where the excitation occurs. The inset shows the time evolution of the oscillations inside and outside the region of parametric instability

The observation of this boomerang shaped feature would constitute strong evidence for the presence of this effect in carbon nanotube single electron transistors (CNTSETs).

## Chapter 6

### Summary

In this thesis, the equations of classical elasticity theory are applied to suspended graphene and nanotube structures with various designs. In the first paper, the equations of motion for circular graphene nanodrums are derived and analyzed. The equations are reduced to a set of coupled Duffing oscillators for the mode amplitudes. Further, a static deformation introduces quadratic coupling terms. Interestingly, the stress field induced by the static deformation is nonuniform, which leads to additional renormalization of the mode frequencies. These renormalizations introduce frequency crossings.

The second paper concerns the dissipation of a graphene beam coupled to an elastic medium. It is found that the coupling between in-plane and out-of-plane motion causes both linear and nonlinear damping to be present in these systems. Although this nonlinear term was found to be too small to dominate the nonlinear response of suspended graphene sheets under realistic assumptions, it can, under certain circumstances, be the dominating dissipation term. More specifically, the ratio between the nonlinear and linear damping terms scale as  $|q_{1,\max}|^2/\bar{q}^2$ , where  $q_{1,\max}$  is the amplitude of the vibrational motion, and  $\bar{q}$  is the static displacement of the graphene sheet. Thus, the nonlinear damping can dominate for small static displacements. The quality factor displays qualitatively different behavior with respect to driving voltage and bias voltage in the two different damping regimes. The quality factors obtained from this mechanism ranges from  $10^4$  to  $10^6$  for the considered geometry, which is consistent with recent experimental findings [66].

In the third paper, the relaxation properties of graphene resonators are investigated further. Specifically, the relaxation and thermalization of a nanodrum due to the nonlinear mode couplings derived in the first paper is considered. An analogy with the famous FPU problem is drawn, and the system is shown to display a metastable state for initial data very far from equilibrium. After the break down of the metastable state, the

energy decays toward equipartition at a rate that is energy dependent. The thermalization due to nonlinear mode couplings is an internal process inherent to the resonator itself, and so constitutes a lower bound on the relaxation rate. Further, the connection between the mode couplings in graphene resonators and the FPU problem suggests that these nanoresonators may be used as test beds for various concepts within nonlinear non equilibrium systems.

In the fourth paper, the bending rigidity of monolayer and bilayer graphene is estimated using suspended graphene sheets that are buckled due to a built-in compressive strain, fabricated and characterized by an experimental group at Gothenburg University. These structures were shown to display a snap-through instability under large enough pressures. Describing the buckled graphene sheet as a shallow elastic shell, the critical pressure could be related to the bending rigidity of the system. The bending rigidity of bilayer graphene was estimated to  $\kappa \approx 30_{-15}^{+20}$  eV, and for monolayers to  $\kappa \sim 7_{-3}^{+4}$  eV.

Finally, the fifth paper concerns a parametric actuation scheme for suspended carbon nanotube single electron transistors (CNTSETs). The strong coupling between the mechanical motion of the nanotube and the occupation of the quantum dot reported previously [78, 79] gives rise to a frequency shift at the degeneracy point. By periodically modulating the source drain voltage, the frequency shift is modulated without introducing direct driving terms into the equation of motion.

In conclusion, this thesis concerns the use of continuum mechanics to model and characterize nonlinear dynamics in mechanical nanostructures. The ability to accurately describe the dynamics of these structure is essential for future applications. This thesis develops and strengthens the theoretical foundation for this type of modeling by connecting the predicted dynamics of the resonators to experimental results. In addition, the possibility of using nanoresonators to further the understanding of nonlinear non equilibrium physics is introduced.

## Appendix A

# Equation of motion for nanobeam

In this appendix, the equations of motion for the vibrational modes of a graphene nanobeam are derived.

I consider a ribbon of width  $b$ , suspended over a trench of length  $l$ . The ribbon is actuated by a homogeneous pressure. The boundary condition for the free edges are that the stresses vanish there,

$$\begin{aligned}\sigma_{xy} &= \frac{\partial \mathcal{F}}{\partial \epsilon_{xy}} = 0 \\ \sigma_{yy} &= \frac{\partial \mathcal{F}}{\partial \epsilon_{yy}} = 0.\end{aligned}\tag{A.1}$$

The first boundary condition gives that  $\epsilon_{xy} = 0$ , indicating an absence of shear strain. The second reads

$$2 \left( \frac{\lambda}{2} + \mu \right) \epsilon_{yy} + \lambda \epsilon_{xx} = 0.\tag{A.2}$$

This means that the transversal ( $\epsilon_{yy}$ ) strain at the boundary is related to  $\epsilon_{xx}$  through the Poisson ratio  $\frac{\lambda}{\lambda+2\mu}$ . Far from the boundary, the transversal strain will vanish. For sufficiently wide beams, this means that the structure can be treated as a quasi one-dimensional structure by setting  $\epsilon_{yy} = 0$ .

The free energy density of the sheet then becomes

$$\mathcal{F} = \frac{T_1}{2} (u_x^2 + u_x w_x^2 + w_x^4/4)\tag{A.3}$$

where  $T_1 = \lambda + 2\mu$ . The equations of motion are obtained from the Euler-Lagrange equations,

$$\begin{aligned}\rho_G \ddot{u} - T_1 u_{xx} &= \frac{T_1}{2} \partial_x (w_x^2) \\ \rho_G \ddot{w} &= \frac{T_1}{2} \partial_x [(2u_x + w_x^2) w_x].\end{aligned}\quad (\text{A.4})$$

Often, suspended graphene structure have rather large internal stresses even in the absence of flexural deformation. This is taken into account in the model by writing  $u_x = \epsilon + \delta u_x$ , where  $\epsilon$  is the strain in the absence of flexural deformation. This introduces a linear term in the equations of motion for the out-of-plane dynamics. Further, the characteristic time scale for in-plane phonons is given by  $\sqrt{\frac{T_1}{\rho_G}} \frac{1}{l}$ , while the time scale for small flexural vibrations is  $\sqrt{\frac{T_1 \epsilon}{\rho_G}} \frac{1}{l}$ . As  $\epsilon \ll 1$ , the in-plane modes will move much faster than the flexural modes, which implies that the in-plane modes can be adiabatically eliminated by setting  $\ddot{u} = 0$  in the equations of motion. Consequently, the equations of motion are

$$\begin{aligned}\delta u_{xx} &= -\frac{1}{2} \partial_x (w_x^2) \\ \rho_G \ddot{w} &= T_0 w_{xx} + \frac{T_1}{2} \partial_x [(2\delta u_x + w_x^2) w_x],\end{aligned}\quad (\text{A.5})$$

where  $T_0 = \epsilon T_1$ , and the boundary conditions are  $w(-l/2) = w(l/2) = \delta u(-l/2) = \delta u(l/2) = 0$ . We note that the linear wave equation is recovered for  $T_0 \gg T_1$ . In most applications however,  $T_0$  is much smaller than  $T_1$ , meaning that the response of a suspended graphene sheet is highly nonlinear. At this point, it is useful to note that the equations can be made dimensionless and parameter free by introducing the scaled variables

$$\tilde{x} = \frac{x}{l}; \quad \tilde{t} = \frac{\sqrt{\epsilon} c_L}{l} t; \quad \tilde{w}^2 = \frac{1}{2} \frac{w^2}{l^2 \epsilon}; \quad \tilde{E} = \frac{E}{2\epsilon^2 c_L^2 \rho l^2} \quad (\text{A.6})$$

where  $c_L^2 = \frac{T_1}{\rho_G}$  is the longitudinal sound velocity of graphene. Skipping the tildes on the scaled variables for convenience, the dimensionless equations of motion becomes

$$\begin{aligned}\delta u_{xx} &= -\frac{1}{2} \partial_x (w_x^2) \\ \ddot{w} &= w_{xx} + \partial_x [(2\delta u_x + w_x^2) w_x],\end{aligned}\quad (\text{A.7})$$

with boundary conditions  $w(-1/2) = w(1/2) = \delta u(-1/2) = \delta u(1/2) = 0$ . An applied pressure can be taken into account by adding a force term on the right hand side of the equation for the out-of-plane motion.

## A.1 Response of nanobeam to static force

In order to address the dynamics of these equations, I will need to analyze the equations in the static limit by setting  $\ddot{w} = 0$ . First, the in-plane equation can easily be solved to obtain the in-plane deformation in terms of the flexural deformation by simply integrating the equation. Then one obtains

$$u_x(x) = -\frac{1}{2} \left( w_x(x)^2 - \int_{-1/2}^{1/2} dx' w_x^2 \right). \quad (\text{A.8})$$

Inserting this into the out-of-plane equation, the equation reads

$$w_{xx} + w_{xx} \int_{-1/2}^{1/2} dx' w_x^2 = 0, \quad (\text{A.9})$$

that is, the nonlinear behavior depends on an average of the flexural deformation. This *nonlocal* feature of the equations of motion is an artifact of the adiabatic elimination of the in-plane dynamics. Next, a static, uniform pressure is applied to the membrane, changing the equation to

$$\left( 1 + \int_{-1/2}^{1/2} dx' w_x^2 \right) w_{xx} = -P_z, \quad (\text{A.10})$$

This equation is solved making the ansatz  $w = 4w(0)(x - 1/2)(x + 1/2)$ , where  $w(0)$  is the flexural deformation at  $x = 0$ . This leads to a cubic relation between the maximal deformation and the applied pressure,

$$8w(0) \left( 1 + \frac{16w(0)^2}{3} \right) = P_z \quad (\text{A.11})$$

which can be solved to obtain the flexural deformation due to a static load  $P_z$ . The maximal deformation is shown as function of the static pressure in figure A.1. For small pressures, the deformation increases linearly, while it increases as  $P_z^{1/3}$  for larger pressures.

An important feature of the beam geometry is that a static deformation gives rise to a uniform renormalization of the stress in the resonator according to (A.10).

## A.2 Dynamical response of nanobeam

Having elucidated the static response of a suspended nanobeam, I will now consider a dynamical pressure, introduced by adding to the static pressure a spatially homogeneous,

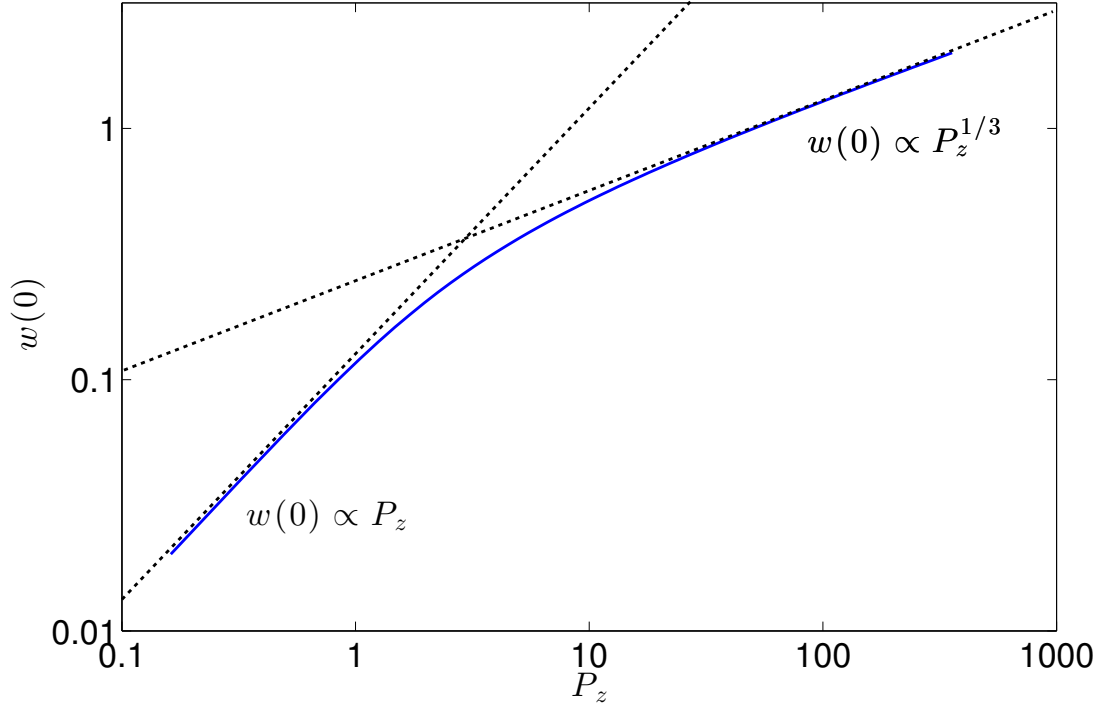


FIGURE A.1: Maximal flexural deformation  $w(0)$  as a function of the applied pressure  $P_z$ . The dotted lines are the corresponding asymptotic scalings.

periodically varying pressure,

$$\ddot{w} - \left(1 + \int_{-1/2}^{1/2} dx' w_x'^2\right) w_{xx} = P_z + p_z \cos \omega t. \quad (\text{A.12})$$

This is analyzed by writing  $w = \bar{w}(x) + \delta w(x, t)$ , where  $\bar{w}$  is the solution to the static problem (A.10). Denoting the integration over the beam by  $\langle \cdot \rangle$ , the equation for the dynamical response  $\delta w$  becomes

$$\delta \ddot{w} - [1 + \langle \bar{w}_x^2 \rangle + \langle 2\bar{w}_x \delta w_x \rangle + \langle \delta w_x^2 \rangle] \delta w_{xx} + [\langle 2\bar{w}_x \delta w_x \rangle + \langle \delta w_x^2 \rangle] \bar{w}_{xx} = p_z \cos \omega t. \quad (\text{A.13})$$

The first term on the right hand side corresponds to a frequency shift, while the second term corresponds to a simple rescaling of the static response due to the instantaneous pressure. This is most easily seen by expanding the equation in the fundamental modes of the linear wave equation on this domain,  $\delta w(x, t) = \sum q_n(t) \phi_n(x)$ , where the mode functions  $\phi_n = \sqrt{2} \cos(n\pi x + (n-1)\pi/2)$  satisfy  $\partial_x^2 \phi_n = -n^2 \pi^2 \phi_n$ ,  $\langle \phi_n \phi_m \rangle = \delta_{nm}$  and  $\langle \partial_x \phi_n \partial_x \phi_m \rangle = n^2 \pi^2 \delta_{nm}$ . Then, the equation of motion for the mode amplitudes becomes

$$\ddot{q}_n + \tilde{\omega}_n^2 q_n + \delta \omega_n^2 \left( q_n + \frac{8w(0)}{n^2 \pi^2} \langle \phi_n \rangle \right) = \langle p_z \phi_n \rangle \cos \omega t, \quad (\text{A.14})$$

with  $\tilde{\omega}_n^2 = n^2\pi^2 (1 + \langle \bar{w}_x^2 \rangle)$  and  $\delta\omega_n(t)^2 = n^2\pi^2 (\sum_m q_m \langle 2\bar{w}_x \partial_x \phi_m \rangle + \pi^2 \sum_m m^2 q_m^2)$ . The static deformation therefore gives rise to a shift in the linear frequency of the resonator, while the nonlinear mode couplings give rise to a fluctuation of the frequency  $\delta\omega_n(t)^2$ .

## Appendix B

# Equation of motion for graphene sheet coupled to elastic substrate

In this appendix, the derivation of the equation for the slowly varying envelope (3.6) of a graphene resonator coupled to a medium is sketched. Starting from (3.4) the stress is divided into a constant part, a part that depends on the in-plane displacement and a part that depends on the out-of-plane displacement,

$$\sigma_{ij} = \sigma_{ij}^0 + \sigma_{ij}^u + \sigma_{ij}^w \quad (\text{B.1})$$

Taking  $\sigma_{ij}^0 = \delta_{ij}\sigma^0$ , the equations of motion for the graphene are modified to

$$\begin{aligned} \rho_G \ddot{\vec{u}} &= \nabla \cdot (\bar{\sigma}^u + \bar{\sigma}^w) + \lambda_\Omega (\vec{u} - \vec{s}_{||,z=0}) \\ \rho_G \ddot{w} &= \sigma^0 \nabla^2 w + \nabla \cdot [(\bar{\sigma}^u + \bar{\sigma}^w) \nabla w] \end{aligned} \quad (\text{B.2})$$

Since  $\bar{\sigma}^u$  is linear in  $u$ , one may formally write the solution to the in-plane problem in terms of a response matrix  $R_{ij}(\vec{x}, \vec{x}', t - t')$ ,

$$u_i = \int d\vec{x}' dt' R_{ij}(\vec{x}, \vec{x}', t - t') \partial_k \sigma_{jk}^w \quad (\text{B.3})$$

The form of the response function  $R_{ij}$  is determined by the geometry of the suspended domain and by the interaction with the substrate.

Next, the out-of-plane motion is expanded in terms of the normal modes of the Laplacian with clamped (Dirichlet) boundary conditions on the edge  $\partial\Omega$  of the suspended domain,

$$w(\vec{x}, t) = \sum_{ij} q_{ij}(t) \phi_{ij}(\vec{x}) \quad (\text{B.4})$$

To keep the calculations transparent, the sheet is assumed to be driven by an external force that excites only the fundamental vibrational mode. The expressions for the out-of-plane motion and the out-of-plane part of the stress becomes

$$\begin{aligned} w(\vec{x}, t) &= q(t)\phi(\vec{x}) \\ \sigma_{ij}^w &= \frac{q(t)^2}{2} \left[ \lambda \delta_{ij} (\phi_{,k}(\vec{x}))^2 + 2\mu \phi_{,i}(\vec{x}) \phi_{,j}(\vec{x}) \right] \end{aligned} \quad (\text{B.5})$$

where the mode function  $\phi(\vec{x})$  have the following properties

$$\begin{aligned} \nabla^2 \phi(\vec{x}) &= -k^2 \phi(\vec{x}) \\ \phi(\vec{x} \in \partial\Omega) &= 0 \\ \langle \phi(\vec{x})^2 \rangle &\equiv \int_{\Omega} d\vec{x} \phi(\vec{x})^2 = A_{\Omega} \end{aligned} \quad (\text{B.6})$$

with  $A_{\Omega}$  being the area of the suspended domain. The equation of motion for the mode amplitude  $q(t)$  then becomes

$$\ddot{q} + \frac{k^2 \sigma^0}{\rho_G} q + \frac{\alpha_0}{\rho_G A_{\Omega}} q^3 + \frac{q}{A_{\Omega} \rho_G} \langle (\nabla \phi)^T \bar{\sigma}^u \nabla \phi \rangle = \frac{f_0 \cos \omega t}{\rho_G A_{\Omega}} \langle \phi \rangle \quad (\text{B.7})$$

where  $k \sqrt{\frac{\sigma^0}{\rho_G}} \equiv \omega_0$  is the resonance frequency of the resonator,  $\alpha_0 \equiv \langle \phi_{,i} \left[ \lambda \delta_{ij} (\phi_{,k})^2 + 2\mu \phi_{,i} \phi_{,j} \right] \phi_{,j} \rangle$  is the Duffing parameter and the driving force  $f(t) = f_0 \cos \omega t$  is introduced.

Inserting the expression for the out-of-plane part of the stress into (B.3), the expression for the in-plane displacement becomes

$$u_i = \frac{1}{2} \int d\vec{x}' dt' R_{ij}(\vec{x}, \vec{x}', t - t') q(t')^2 \partial_k \left[ \lambda \delta_{jk} (\phi_{,l}(\vec{x}))^2 + 2\mu \phi_{,j}(\vec{x}) \phi_{,k}(\vec{x}) \right] \quad (\text{B.8})$$

For external forces that are periodic with frequency  $\omega$  close to  $\omega_0$ , the amplitude of the out-of-plane motion can be written as

$$q(t) = q_0 + \frac{1}{2} (q_1(t) e^{i\omega t} + q_1^*(t) e^{-i\omega t}); \quad \dot{q} = \frac{i\omega}{2} (q_1(t) e^{i\omega t} - q_1^*(t) e^{-i\omega t}) \quad (\text{B.9})$$

where  $q_0$  is the static response and  $q_1$  is a slowly varying function of time.

At this point, it is worthwhile to consider the time and length scales involved in the problem. Disregarding the graphene-substrate coupling for a moment, the wavelength of the emitted in-plane phonons will be of the order  $\lambda_{ph} \sim \frac{c_G}{2\pi\omega_0} \sim l \sqrt{\frac{T_1}{\sigma^0}}$ , where  $c_G$  is the sound velocity of graphene,  $l$  is a characteristic length scale of the suspended domain and  $T_1 = \lambda + 2\mu$  has been introduced previously. Since  $\frac{T_1}{\sigma^0} \sim 10^3$  for typical graphene

sheets fabricated by exfoliation, the wavelength of the emitted phonon will be much longer than the size of the suspended domain. The propagation time for such a phonon across the suspended domain is similarly much shorter than the period of oscillation for the out-of-plane motion. Then, the slowly oscillating  $q_1$  may be pulled out of the integral expression for the in-plane displacement, resulting in

$$\begin{aligned}
 u_i = \frac{1}{2} \left[ \left( q_0^2 + \frac{|q_1|^2}{2} \right) \int d\vec{x}' dt' R_{ij}(\vec{x}, \vec{x}', t - t') \mathcal{D}_j[\phi(\vec{x}')] + \right. \\
 q_0 q_1 e^{i\omega t} \int d\vec{x}' dt' R_{ij}(\vec{x}, \vec{x}', t - t') e^{i\omega(t'-t)} \mathcal{D}_j[\phi(\vec{x}')] + \\
 \left. \frac{q_1^2}{4} e^{2i\omega t} \int d\vec{x}' dt' R_{ij}(\vec{x}, \vec{x}', t - t') e^{2i\omega(t'-t)} \mathcal{D}_j[\phi(\vec{x}')] + c.c \right] \quad (\text{B.10})
 \end{aligned}$$

where  $\mathcal{D}_j[\phi] = \partial_k \left[ \lambda \delta_{jk} (\phi_{,l}(\vec{x}))^2 + 2\mu \phi_{,j}(\vec{x}) \phi_{,k}(\vec{x}) \right]$ .

Note that the time integrals in the above expression can be expressed as Fourier transforms of the response function,  $\tilde{R}_{ij}(\vec{x}, \vec{x}', \Omega)$ . Each of the integrals correspond to a specific frequency component of the in-plane motion. Writing  $u_i(\vec{x}, t) = u_{0i} + \frac{1}{2} (u_{1i}(\vec{x}, t)e^{i\omega t} + u_{1i}^*(\vec{x}, t)e^{-i\omega t}) + \frac{1}{2} (u_{2i}(\vec{x}, t)e^{2i\omega t} + u_{2i}^*(\vec{x}, t)e^{-2i\omega t})$  these different components are given by

$$\begin{aligned}
 u_{0i} &= \frac{1}{2} \left( q_0^2 + \frac{|q_1|^2}{2} \right) \varphi_i(\vec{x}, 0) \\
 u_{1i} &= q_0 q_1 \varphi_i(\vec{x}, -\omega) \\
 u_{2i} &= \frac{q_1^2}{4} \varphi_i(\vec{x}, -2\omega) \quad (\text{B.11})
 \end{aligned}$$

where  $\varphi_i(\vec{x}, -\Omega) \equiv \int d\vec{x}' \tilde{R}_{ij}(\vec{x}, \vec{x}', -\Omega) \mathcal{D}_j[\phi(\vec{x}')]$ . The in-plane stress can consequently be written as

$$\begin{aligned}
 \sigma_{ij}^u &= \frac{1}{2} \left( q_0^2 + \frac{|q_1|^2}{2} \right) \tilde{\sigma}_{ij}^u(0) + \\
 & q_0 q_1 \frac{1}{2} (\tilde{\sigma}_{ij}^u(\omega) e^{i\omega t} + \tilde{\sigma}_{ij}^{u*}(\omega) e^{-i\omega t}) \\
 & \frac{q_1^2}{4} \frac{1}{2} (\tilde{\sigma}_{ij}^u(2\omega) e^{2i\omega t} + \tilde{\sigma}_{ij}^{u*}(2\omega) e^{-2i\omega t}) \quad (\text{B.12})
 \end{aligned}$$

where the different frequency components  $\tilde{\sigma}_{ij}^u(k\omega)$ ,  $k = 0, 1, 2$  are given by

$$\tilde{\sigma}_{ij}^u(k\omega) = \lambda \delta_{ij} \varphi_{l,l}(\vec{x}, -k \cdot \omega) + 2\mu \varphi_{i,j}(\vec{x}, -k \cdot \omega) \quad (\text{B.13})$$

Inserting these expressions into the equation for the out-of-plane motion and integrating over one period, the equation becomes

$$\begin{aligned}
 i\omega\dot{q}_1 + \frac{1}{2} \left( \omega_0^2 - \omega^2 + 3\frac{\alpha_0}{m}q_0^2 \right) q_1 + \frac{3}{8} \frac{\alpha_0}{m} |q_1|^2 q_1 + \frac{1}{2m} q_0^2 q_1 \langle (\nabla\phi)^T \tilde{\sigma}^u(\omega) \nabla\phi \rangle + \\
 \frac{1}{4m} q_1 \left( q_0^2 + \frac{|q_1|^2}{2} \right) \langle (\nabla\phi)^T \tilde{\sigma}^u(0) \nabla\phi \rangle + \\
 \frac{1}{4m} \frac{|q_1|^2 q_1}{4} \langle (\nabla\phi)^T \tilde{\sigma}^u(2\omega) \nabla\phi \rangle = \frac{f_0}{2m} \langle \phi \rangle, \tag{B.14}
 \end{aligned}$$

where  $m \equiv A_\Omega \rho_G$  is the resonator mass.

Depending on the form of the response function  $R(x, x', t - t')$ , the overlap integrals will have both real and imaginary parts. The real parts will renormalise the resonance frequency and Duffing parameter, while the imaginary parts correspond to dissipation. The term containing  $\tilde{\sigma}^u(\omega)$  is linear in the out-of-plane amplitude, and corresponds to a linear viscous damping. On the other hand, the term containing  $\tilde{\sigma}^u(2\omega)$  multiplies  $q_1 |q_1|^2$  and corresponds to an amplitude dependent, or nonlinear, damping. The importance of this damping is determined partly by the ratio between the nonlinear damping and the linear damping, and partly by the ratio between the nonlinear damping and the Duffing parameter. To separate the terms, the following notation is introduced,

$$\begin{aligned}
 \gamma &= \frac{1}{\omega} q_0^2 \text{Im} \{ \langle (\nabla\phi)^T \tilde{\sigma}^u(\omega) \nabla\phi \rangle \} \\
 \eta &= \frac{1}{2\omega} \text{Im} \{ \langle (\nabla\phi)^T \tilde{\sigma}^u(2\omega) \nabla\phi \rangle \} \\
 \frac{3}{8} \tilde{\alpha} &= \frac{3}{8} \alpha + \frac{1}{8} \text{Re} \{ 2 \langle (\nabla\phi)^T \tilde{\sigma}^u(0) \nabla\phi \rangle + \langle (\nabla\phi)^T \tilde{\sigma}^u(2\omega) \nabla\phi \rangle \} \\
 \tilde{\omega}_0^2 &= \omega_0^2 + \left( 3 \frac{\alpha}{m} + \frac{1}{4m} \langle (\nabla\phi)^T \tilde{\sigma}^u(0) \nabla\phi \rangle + \frac{1}{2m} \text{Re} \{ \langle (\nabla\phi)^T \tilde{\sigma}^u(\omega) \nabla\phi \rangle \} \right) q_0^2. \tag{B.15}
 \end{aligned}$$

The equation of motion for the slowly varying amplitude can then be written as

$$i\omega\dot{q}_1 + \frac{1}{2} (\tilde{\omega}_0^2 - \omega^2) q_1 + \frac{3}{8} \frac{\tilde{\alpha}}{m} |q_1|^2 q_1 + i \frac{1}{2m} \gamma \omega q_1 + i \frac{1}{8m} \eta \omega |q_1|^2 q_1 = \frac{f_0}{2m} \langle \phi \rangle. \tag{B.16}$$

## Appendix C

# Scaling of snap-through voltage for drum and beam structures

Assume that a small pressure, well below the critical pressure, is applied to a shallow spherical shell of radius  $R$ . The shell will respond by locally becoming "flatter" at the top of the shell. In other words, in a region of width  $d$ , the radius of curvature increases from  $R$  to  $R' > R$  (figure C.2). As the radius of curvature  $R'$  increases, the graphene within the flattened region is compressed. At some pressure, the deformed part of the shell will be completely flat. Deforming the shell further, the compressive strain will be released until the deformed part of the shell form a mirror image of its original shape. Then, both the bending and stretching contributions to the energy will be equal to the undeformed shell, apart from a considerable bending in a region close to the edge of the deformed region. In other words, the deformation of a shallow shell will be qualitatively different for small and large applied pressures. It turns out that the latter configuration is unstable under an applied pressure. The pressure at which the transition between the two types of deformation occurs will therefore be the critical pressure. A schematic depiction of the process is given in figure C.1.

The deformation at small pressures is parametrized by the width and depth of the deformation according to figure C.2. We aim at finding these parameters by minimizing the free energy of the system.

The elastic energy is divided into two parts,  $U_{tot} = U_b + U_s$ . The bending energy density is given by

$$u_b \sim \kappa(\xi'')^2, \tag{C.1}$$

where  $\xi$  is the deflection of the shell in the radial direction, and the differentiation is with respect to a length element  $ds$  in the meridial direction. Since the deflection changes by

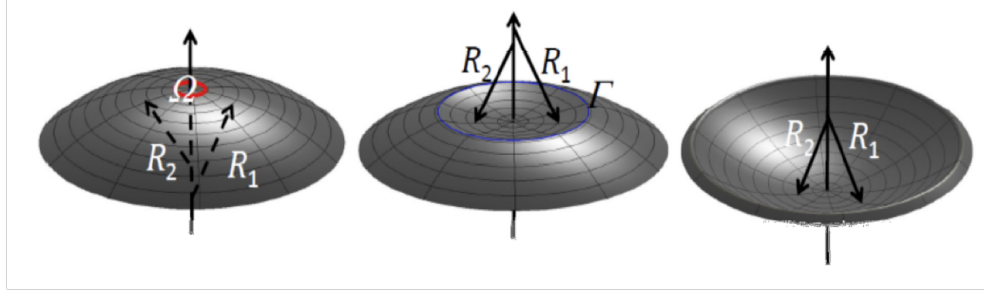


FIGURE C.1: A schematic view of the process of snap through. Left: For small pressures a local deformation is formed in the region denoted  $\Omega$ . Middle: When the critical pressure is reached, it becomes energetically favorable to form a concave region where the elastic energy is confined to a narrow region  $\Gamma$ . Right: This concave region is elastically unstable. As a result, the deformation propagates outward, and the sheet snaps through.

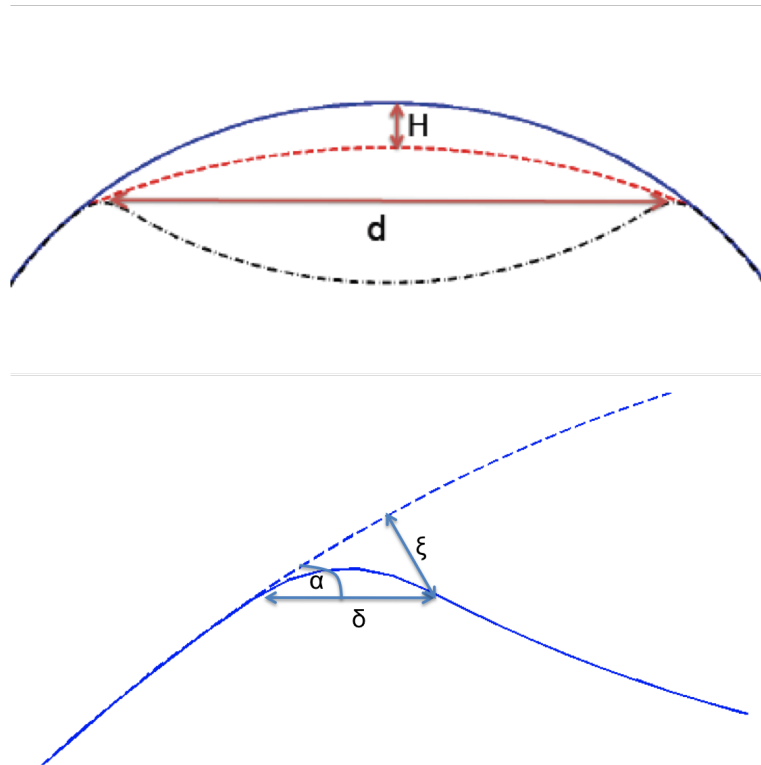


FIGURE C.2: Top: Shells under external pressure display two qualitatively different regions of deformation, indicated in the figure by the dashed and dash-dotted line. At low pressures, the shell will locally flatten, decreasing the local curvature. For large pressures, the deformed part of the shell will form a mirror image of its undeformed counterpart. The main contribution to the elastic energy will then be contained in a narrow region close to the edge of the deformed region. Bottom: Close-up of the edge of the deformation for large pressures. The edge region can be parametrized by a width  $\delta$  and an angle  $\alpha$ .

$H$  over a distance  $d$ , the second derivative can be approximated by

$$\xi'' \sim \frac{H}{d^2}. \quad (\text{C.2})$$

The bending energy density thus becomes

$$u_b \sim \kappa \frac{H^2}{d^4}. \quad (\text{C.3})$$

As for the stretching energy density, it is given by

$$u_s \sim T \epsilon^2, \quad (\text{C.4})$$

where  $\epsilon$  is the strain. For a spherical shell, the relative elongation of the equator due to a homogeneous radial displacement  $\xi$  is  $\frac{2\pi\xi}{2\pi R} = \frac{\xi}{R}$ . Hence, the strain is  $\epsilon = \frac{\xi}{R} \sim \frac{H}{R}$ ,

$$u_s \sim T \frac{H^2}{R^2}. \quad (\text{C.5})$$

The total elastic energy is the energy density times the area of the bulge, which scales as  $d^2$ ,

$$U_{tot} \sim d^2 (u_b + u_s) = \kappa \frac{H^2}{d^2} + T \frac{H^2 d^2}{R^2}. \quad (\text{C.6})$$

Note that the bending energy decreases with the bulge size  $d$ , while the stretching energy increases with  $d$ . To determine the equilibrium shape of the shell, it is clear that both bending and stretching must be taken into account.

To find  $d$ , we consider Gibbs free energy,

$$G = U - p\Delta V, \quad (\text{C.7})$$

where  $p$  is the pressure and  $\Delta V$  is the change in volume due to the deformation. This volume scales as  $\Delta V \sim Hd^2$ , so

$$G \sim \left( \frac{TH^2}{R^2} - pH \right) d^2 + \kappa \frac{H^2}{d^2}, \quad (\text{C.8})$$

so the effect of the pressure is to renormalize the parameter  $T$  to  $\tilde{T} = T - \frac{pR^2}{H}$ . Minimizing the free energy with respect to  $d$  we find

$$0 = \frac{\partial G}{\partial d} \sim \tilde{T} \frac{dH^2}{R^2} - \kappa \frac{H^2}{d^3} \Rightarrow d \sim \left( \frac{\kappa}{\tilde{T}} \right)^{1/4} R^{1/2}. \quad (\text{C.9})$$

Inserting this into the free energy, we find

$$U_{tot} \sim \sqrt{\kappa \tilde{T}} \frac{H^2}{R}, \quad (\text{C.10})$$

and the work done by the pressure is

$$p\Delta V \sim pHR \frac{\kappa^{1/2}}{\tilde{T}^{1/2}}. \quad (\text{C.11})$$

Once again minimizing Gibbs free energy, this time with respect to  $H$ , we find

$$0 = \frac{\partial G}{\partial H} = \left( \frac{H}{R} \sqrt{\kappa \tilde{T}} - pR \frac{\kappa^{1/2}}{\tilde{T}^{1/2}} \right) + \left( \frac{H^2}{R} \frac{\kappa^{1/2}}{\tilde{T}^{1/2}} + pHR \frac{\kappa^{1/2}}{\tilde{T}^{3/2}} \right) \frac{\partial \tilde{T}}{\partial H}. \quad (\text{C.12})$$

Inserting  $\frac{\partial \tilde{T}}{\partial H} = p \frac{R^2}{H^2}$ , we find

$$0 = \left( \frac{H}{R} \sqrt{\kappa \tilde{T}} - pR \frac{\kappa^{1/2}}{\tilde{T}^{1/2}} \right) + pR \frac{\kappa^{1/2}}{\tilde{T}^{1/2}} + \frac{p^2 R^3}{H} \frac{\kappa^{1/2}}{\tilde{T}^{3/2}}, \quad (\text{C.13})$$

which gives

$$H \sim \frac{pR^2}{\tilde{T}} = \frac{pR^2}{T - \frac{pR^2}{H}}. \quad (\text{C.14})$$

Solving this equation for  $H$  finally gives

$$H \sim \frac{pR^2}{T}. \quad (\text{C.15})$$

This is the scaling of the depth of the deformation as a function of the applied pressure. The situation described above ceases to be valid if the forces on the membrane are so large that the shape of the membrane changes considerably. In this case, we assume that the bulge forms a mirror reflection of its original surface in a plane perpendicular to the symmetry axis. This means that well inside the bulge, the curvature of the deformed shell is opposite in sign but equal in magnitude to the curvature of the original surface, and hence the free energy density here remains unaffected. Instead, the major part of the change in free energy will be concentrated to a narrow strip of width  $\delta$  around the edge of the bulge. The radius of the bulge is denoted  $r$ , and its depth  $H$ . We start by finding  $\delta$ , once again through minimization of Gibbs free energy.

The bending energy density is again given by

$$u_b \sim \kappa \frac{\xi^2}{\delta^4}, \quad (\text{C.16})$$

and the stretching by

$$u_s \sim T \frac{\xi^2}{R^2}. \quad (\text{C.17})$$

The area of the bending strip scales as  $r\delta$ , so the total elastic energy becomes

$$U_{tot} = r\delta \left( \kappa \frac{\xi^2}{\delta^4} + T \frac{\xi^2}{R^2} \right). \quad (\text{C.18})$$

The deflection  $\xi$  is determined geometrically. With the notation defined in figure C.2, we have  $\xi = \delta \sin \alpha \approx \delta \frac{r}{R}$ .

The total elastic energy thus becomes

$$U_{tot} \sim \kappa \frac{r^3}{R^2 \delta} + T \frac{r^3 \delta^3}{R^4}. \quad (\text{C.19})$$

The work done by the pressure is again

$$W = p\Delta V \sim pHr^2. \quad (\text{C.20})$$

Note that the work done by the pressure does not depend on the width of the bending strip  $\delta$ ; hence, in determining  $\delta$  only the elastic free energy needs to be considered,

$$0 = \frac{\partial U_{tot}}{\partial \delta} \sim r^3 \left( T \frac{\delta^2}{R^4} - \kappa \frac{1}{R^2 \delta^2} \right) \rightarrow \delta \sim \frac{\kappa^{1/4}}{T^{1/4}} R^{1/2}. \quad (\text{C.21})$$

Before we write down Gibbs free energy, we note that  $r$  and  $H$  are related geometrically through  $r^2 \sim RH$ . Then, minimizing Gibbs free energy with respect to  $H$  we find

$$0 = \frac{\partial G}{\partial H} = \frac{\kappa^{3/4} T^{1/4} H^{1/2}}{R} - pRH, \quad (\text{C.22})$$

which gives

$$H \sim \frac{\kappa^{3/2} T^{1/2}}{R^4 p^2}. \quad (\text{C.23})$$

The physical interpretation of this result is that if one decreases the pressure, the bulge will increase in size; this indicates that the structure is unstable. Indeed, calculating the second derivative of Gibbs free energy one finds

$$\frac{\partial^2 G}{\partial H^2} = \frac{\kappa^{3/4} T^{1/4}}{2RH^{1/2}} - pR = -\frac{pR}{2} < 0, \quad (\text{C.24})$$

meaning that this value of  $H$  corresponds to a maximum of Gibbs free energy, not a minimum. Larger bulges will grow on their own accord, while smaller bulges will decrease. It is therefore expected that until the critical bulge size  $H$  is reached, the deformation is well described by the scaling derived in the previous section,

$$H \sim \frac{pR^2}{T}. \quad (\text{C.25})$$

So at what pressure does  $H$  reach its critical value? We set  $H = H_{cr}$ , giving

$$\frac{p_{cr}R^2}{T} = \frac{\kappa^{3/2}T^{1/2}}{R^4p_{cr}^2} \Rightarrow p_{cr} \sim \frac{\sqrt{\kappa T}}{R^2}, \quad (\text{C.26})$$

giving the correct scaling behavior.

The same method can be applied to doubly clamped beams with principal radii of curvature  $R_x$  and  $R_y$ . In this case, the stretching energy is expected to scale with the Gaussian curvature, so

$$u_s = T \frac{\xi^2}{R_x R_y}. \quad (\text{C.27})$$

Hence, for small deflections it is sufficient to do the substitution  $R^2 \rightarrow R_x R_y$ , resulting in

$$H \sim \frac{p R_x R_y}{T}. \quad (\text{C.28})$$

For large deflections, the situation is slightly more intricate. One can no longer assume that the bulge formed in the ribbon is closed by a simply connected curve as depicted in figure C.1. Let us instead investigate the limit where this edge consists of two parallel lines, separated by a distance  $2r$ . Again, we start by determining the width of the edge region,  $\delta$  by minimizing the free energy. The bending energy density is still

$$u_b \sim \kappa \frac{\xi^2}{\delta^4}, \quad (\text{C.29})$$

while the stretching energy scales with the Gaussian curvature, as argued above,

$$u_s \sim T \frac{\xi^2}{R_x R_y}. \quad (\text{C.30})$$

The same geometrical argument as for the fully clamped structures gives for the deflection

$$\xi \sim \delta \frac{r}{R_x}. \quad (\text{C.31})$$

The area of the width region scales as  $D\delta$ , where  $D$  is the width of the ribbon, so the total elastic energy becomes

$$U_{tot} \sim D\delta \left( \kappa \frac{r^2}{\delta^2 R_x^2} + T \frac{r^2 \delta^2}{R_x^3 R_y} \right). \quad (\text{C.32})$$

Minimizing with respect to  $\delta$  gives

$$\delta \sim \left( \frac{\kappa}{T} R_x R_y \right)^{1/4}, \quad (\text{C.33})$$

where I have used  $r^2 \sim HR_x$ . Inserting this into the elastic energy yields

$$U_{tot} \sim \frac{\kappa^{3/4} T^{1/4} H D}{R_x^{5/4} R_y^{1/4}}. \quad (\text{C.34})$$

The work done by the pressure is

$$W = p\Delta V \sim p H r D \sim p D H^{3/2} R_x^{1/2}, \quad (\text{C.35})$$

again using  $r^2 \sim HR_x$ . Once again differentiating Gibbs free energy with respect to  $H$  one finds

$$H_{cr} \sim \frac{\kappa^{3/2} T^{3/2}}{R_x^{7/2} R_y^{1/2} p^2}, \quad (\text{C.36})$$

where the subscript  $cr$  indicates that this is again the critical deformation of the shell. Using the scaling for small deformations found previously,  $H \sim \frac{p R_x R_y}{T}$ , one obtains the critical pressure

$$p_{cr} \sim \frac{\kappa^{1/4} T^{1/4}}{R_x^{3/2} R_y^{1/2}}. \quad (\text{C.37})$$

If the pressure is applied electrostatically, we expect that  $p \sim V^2$ , meaning that the critical voltage scales as

$$V_{cr} \sim \frac{\kappa^{1/4} T^{1/4}}{R_x^{3/4} R_y^{1/4}}. \quad (\text{C.38})$$

# Bibliography

- [1] A. H. Castro Neto, F. Guinea, N. M. R. Peres, K. S. Novoselov, and A. K. Geim. The electronic properties of graphene. *Rev. Mod. Phys.*, 81:109–162, Jan 2009.
- [2] E. Fermi, J. R. Pasta, and S. Ulam. Studies of nonlinear problems. Technical report, Los Alamos Scientific Laboratory, 1955.
- [3] Y. Imry. *Introduction to mesoscopic physics*. Oxford University Press, New York, 2002.
- [4] R. Kubo, M. Toda, and N. Hashitsume. *Statistical Physics II*. Springer, 1978.
- [5] G. E. Moore. Cramming more components onto integrated circuits. *Electronics*, 38(8), 1965.
- [6] C. Joachim, J. K. Gimzewski, and A. Aviram. Electronics using hybrid-molecular and mono-molecular devices. *Nature*, 408(6812):541–548, 11 2000.
- [7] R. Feynman. There’s plenty of room at the bottom. *Engineering and Science*, pages 22–36, 1960.
- [8] H. W. Kroto, J. R. Heath, S. C. O’Brien, R. F. Curl, and R. E. Smalley. C60: Buckminsterfullerene. *Nature*, 318(6042):162–163, 11 1985.
- [9] S. Iijima and T. Ichihashi. Single-shell carbon nanotubes of 1-nm diameter. *Nature*, 363(6430):603–605, 06 1993.
- [10] M. Monthioux and V. L. Kuznetsov. Who should be given the credit for the discovery of carbon nanotubes? *Carbon*, 44(9):1621 – 1623, 2006. ISSN 0008-6223.
- [11] K. S. Novoselov, A. K. Geim, S. V. Morozov, D. Jiang, Y. Zhang, S. V. Dubonos, I. V. Grigorieva, and A. A. Firsov. Electric field effect in atomically thin carbon films. *Science*, 306(5696):666–669, 2004.
- [12] A. N. Obraztsov. Chemical vapour deposition: Making graphene on a large scale. *Nat Nano*, 4(4):212–213, 04 2009.

- [13] A. S. Mayorov, R. V. Gorbachev, S. V. Morozov, L. Britnell, R. Jalil, L. A. Ponomarenko, P. Blake, K. S. Novoselov, K. Watanabe, T. Taniguchi, and A. K. Geim. Micrometer-scale ballistic transport in encapsulated graphene at room temperature. *Nano Letters*, 11(6):2396–2399, 2011.
- [14] L. A. Ponomarenko, A. K. Geim, A. A. Zhukov, R. Jalil, S.V. Morozov, K. S. Novoselov, I. V. Grigorieva, E. H. Hill, V. V. Cheianov, I. V. Falko, K. Watanabe, T. Taniguchi, and R. V. Gorbachev. Tunable metal-insulator transition in double-layer graphene heterostructures. *Nature Physics*, 2011.
- [15] K. S. Novoselov, V. I. Falko, L. Colombo, P. R. Gellert, M. G. Schwab, and K. Kim. A roadmap for graphene. *Nature*, 490(7419):192–200, 10 2012.
- [16] L. Britnell, R. V. Gorbachev, R. Jalil, B. D. Belle, F. Schedin, A. Mishchenko, T. Georgiou, M. I. Katsnelson, L. Eaves, S. V. Morozov, N. M. R. Peres, J. Leist, A. K. Geim, K. S. Novoselov, and L. A. Ponomarenko. Field-effect tunneling transistor based on vertical graphene heterostructures. *Science*, 335(6071):947–950, 2012.
- [17] T. Georgiou, R. Jalil, B. D. Belle, L. Britnell, R. V. Gorbachev, S. V. Morozov, Y.-J. Kim, A. Gholinia, S. J. Haigh, O. Makarovskiy, L. Eaves, L. A. Ponomarenko, A. K. Geim, K. S. Novoselov, and A. Mishchenko. Vertical field-effect transistor based on graphene-ws2 heterostructures for flexible and transparent electronics. *Nat Nano*, 8(2):100–103, 02 2013.
- [18] X. Wang, L. Zhi, and K. Mullen. Transparent, conductive graphene electrodes for dye-sensitized solar cells. *Nano Letters*, 8(1):323–327, 2008.
- [19] F. Bonaccorso, Z. Sun, T. Hasan, and A. C. Ferrari. Graphene photonics and optoelectronics. *Nat Photon*, 4(9):611–622, 09 2010.
- [20] F. Schedin, A. K. Geim, S. V. Morozov, E. W. Hill, P. Blake, M. I. Katsnelson, and K. S. Novoselov. Detection of individual gas molecules adsorbed on graphene. *Nat Mater*, 6(9):652–655, 09 2007.
- [21] Y. Shao, J. Wang, H. Wu, J. Liu, I.A. Aksay, and Y. Lin. Graphene based electrochemical sensors and biosensors: A review. *Electroanalysis*, 22(10):1027–1036, 2010. ISSN 1521-4109.
- [22] S. K. Min, W. Y. Kim, Y. Cho, and K. S. Kim. Fast dna sequencing with a graphene-based nanochannel device. *Nat Nano*, 6(3):162–165, 03 2011.
- [23] J. S. Bunch, A. M. van der Zande, S. S. Verbridge, I. W. Frank, D. M. Tanenbaum, J. M. Parpia, H. G. Craighead, and P. L. McEuen. Electromechanical resonators from graphene sheets. *Science*, 315(5811):490–493, 2007.

- [24] J. Atalaya, J. M. Kinaret, and A. Isacsson. Nanomechanical mass measurement using nonlinear response of a graphene membrane. *EPL*, 91(4):48001, 2010.
- [25] V. C. Sanchez, A. Jachak, R. H. Hurt, and A. B. Kane. Biological interactions of graphene-family nanomaterials – an interdisciplinary review. *Chem Res Toxicol.*, 25(1):15–34, 2012.
- [26] R. H. Baughman, A. A. Zakhidov, and W. A. de Heer. Carbon nanotubes—the route toward applications. *Science*, 297(5582):787–792, 2002.
- [27] H.-Y. Chiu, P. Hung, H. W. Ch. Postma, and M.x Bockrath. Atomic-scale mass sensing using carbon nanotube resonators. *Nano Lett.*, 8:4342–4346, 2008.
- [28] Y. T. Yang, C. Callegari, X. L. Feng, K. L. Ekinici, and M. L. Roukes. Zeptogram-scale nanomechanical mass sensing. *Nano Lett.*, 6(4):584–586, 2006.
- [29] J. M. Kinaret, T. Nord, and S. Viefers. A carbon nanotube-based nanorelay. *Appl.Phys.Lett*, 82:1287, 2003.
- [30] H. J. Hwang and J. W. Kang. Carbon-nanotube-based nanoelectromechanical switch. *Physica E*, 27:163, 2005.
- [31] A. Isacsson, J. M. Kinaret, and R. Kaunisto. Nonlinear resonance in a three-terminal carbon nanotube resonator. *Nanotech.*, 18, 2007.
- [32] V. Sazonova, Y. Yaish, H. Ustunel, D. Roundy, T. A. Arias, and P. L. McEuen. A tunable carbon nanotube electromechanical oscillator. *Nature*, 431(7006):284–287, 09 2004.
- [33] T. Rueckes, K. Kim, E. Joselevich, G. Y. Tseng, C.-L. Cheung, and C. M. Lieber. Carbon nanotube-based nonvolatile random access memory for molecular computing. *Science*, 289(5476):94–97, 2000.
- [34] C Stampfer, A. Jungen, R Linderman, D. Obergfell, S. Roth, and C Hierold. Nano-electromechanical displacement sensing based on single-walled carbon nanotubes. *Nano Lett.*, 6(7):1449–1453, 2006.
- [35] K.C.Schwab and M.L.Roukes. Putting mechanics into quantum mechanics. *Physics Today*, 2005.
- [36] M. D. LaHaye, O. Buu, B. Camarota, and K. C. Schwab. Approaching the quantum limit of a nanomechanical resonator. *Science*, 304(5667):74–77, 2004.

- [37] A. D. O’Connell, M. Hofheinz, M. Ansmann, Radoslaw C. Bialczak, M. Lenander, Erik Lucero, M. Neeley, D. Sank, H. Wang, M. Weides, J. Wenner, John M. Martinis, and A. N. Cleland. Quantum ground state and single-phonon control of a mechanical resonator. *Nature*, 464:697–703, 2010.
- [38] L. Landau and E.M. Lifschitz. *Theory of Elasticity*, volume 7. Elsevier, 3 edition, 1986.
- [39] D. Garcia-Sanchez, A. M. van der Zande, A. S. Paulo, B. Lassagne, P. L. McEuen, and A. Bachtold. Imaging mechanical vibrations in suspended graphene sheets. *Nano Lett.*, 8:1399–1403, 2008.
- [40] S. Y. Kim and H. S. Park. The importance of edge effects on the intrinsic loss mechanisms of graphene nanoresonators. *Nano Lett.*, 9(3):969–974, 2009.
- [41] A. O. Caldeira and A. J. Leggett. Quantum tunneling in a dissipative system. *Annals of Physics*, 149, 1983.
- [42] M. Dykman and M. Krivoglaz. Theory of nonlinear oscillator interacting with a medium. *Soviet Scientific Reviews, Section A, Physics Reviews*, 5:265—441, 1984.
- [43] L. Casetti, C. Clementi, and M. Pettini. Riemannian theory of hamiltonian chaos and lyapunov exponents. *Phys. Rev. E*, 54(6):5969–5984, 1996.
- [44] L. E. Reichl. *A Modern Course in Statistical Physics*. John Wiley and Sons, 1998.
- [45] J. Ford. The fermi-pasta-ulam problem: Paradox turns discovery. *Physics Reports*, 213(5):271–310, 1992.
- [46] M. Pettini, L. Casetti, M. Cerrutti-Sola, R. Franzosi, and E. G. Cohen. Weak and strong chaos in fermi-pasta-ulam models and beyond. *Chaos*, 15(1), 2005.
- [47] G. P. Berman and F. M. Izrailev. The fermi-pasta-ulam problem: fifty years of progress. *Chaos*, 15(1), 2005.
- [48] G. Gallavotti, editor. *The Fermi-Pasta-Ulam problem*, volume 728. Springer, 2008.
- [49] N. J. Zabusky and M. D. Kruskal. Interaction of ”solitons” in a collisionless plasma and the recurrence of initial states. *Phys. Rev. Lett.*, 15(6):240–243, 1965.
- [50] D. Bambusi and A. Ponno. On metastability in fpu. *Commun. Math. Phys.*, 264: 539–561, 2006.
- [51] F.M. Izrailev and B. V. Chirikov. Statistical properties of a nonlinear spring. *Soviet Physics Doklady*, 11(1):30–32, 1966.

- [52] R. Livi, M. Pettini, S. Ruffo, M. Sparpaglione, and A. Vulpiani. Equipartition threshold in nonlinear large hamiltonian systems: the fermi-pasta-ulam model. *Phys. Rev. A*, 31(2):1039–1044, 1984.
- [53] M. Pettini and M. Cerrutti-Sola. Strong stochasticity threshold in nonlinear large hamiltonian systems: Effect on mixing times. *Phys. Rev. A*, 44(2):975–987, 1991.
- [54] M. Pettini. Geometrical hints for a nonperturbative approach to hamiltonian dynamics. *Phys. Rev. E*, 47(2):828–850, 1992.
- [55] M. Cerrutti-Sola and M. Pettini. Geometric descripton of chaos in two-degrees-of-freedom hamiltonian systems. *Phys. Rev. E*, 53(1):179–188, 1995.
- [56] L. Casetti, M. Pettini, and E. G. D. Cohen. Geometric approach to hamiltonian dynamics and statistical mechanics. *Physics Reports*, 337:237–341, 200.
- [57] L. Casetti, R. Livi, and M. Pettini. Gaussian model for chaotic instability of hamiltonian flows. *Phys. Rev. Lett.*, 74(3):375–378, 1993.
- [58] E. Calderon, L. Horwitz, R. Kupferman, and S. Shnider. On the geometric formulation of hamiltonian dynamics. *Chaos*, 23(1), 2013.
- [59] L. Casetti and M. Pettini. Analytic computation of the strong stochasticity threshold in hamiltonian dynamics using riemannian geometry. *Phys. Rev. E*, 48(6):4320–4332, 1993.
- [60] R. Lifshitz and M.C. Cross. *Nonlinear Dynamics of Nanomechanical and Micromechanical Resonators*, chapter 1. Wiley-VCH, 2008.
- [61] A. H. Nayfeh and D. T. Mook. *Nonlinear Oscillations*. Wiley-VCH, 1995.
- [62] B. N. J. Persson. Theory of rubber friction and contact mechanics. *J. Chem. Phys.*, 115(8):3840–3861, 2001.
- [63] A. A. Maradudin and D. L. Mills. The attenuation of rayleigh surface waves by surface roughness. *Appl. Phys. Lett*, 28(573-575), 1976.
- [64] J. D. Jackson. *Classical Electrodynamics*. John Wiley and Sons, 3rd edition, 1999.
- [65] B. N. J. Persson and H. Ueba. Heat transfer between weakly coupled systems: Graphene on a-sio2. *EPL*, 2010.
- [66] A. Eichler, J. Moser, J. Chaste, M. Zdrojek, I. Wilson-Rae, and A. Bachtold. Nonlinear damping in mechanical resonators made from carbon nanotubes and graphene. *Nat Nano*, 6(6):339–342, 06 2011.

- [67] A. W. Barnard, V. Sazonova, A. M. van der Zande, and P. L. McEuen. Entropic spectral broadening in carbon nanotube resonators. arXiv:1110.1517, 2011.
- [68] R. A. Barton, B. Ilic, A. M. van der Zande, W. S. Whitney, Paul L. McEuen, Jeevak M. Parpia, and Harold G. Craighead. High, size-dependent quality factor in an array of graphene mechanical resonators. *Nano Letters*, 11(3):1232–1236, 2011.
- [69] J. Atalaya, A. Isacsson, and J. M. Kinaret. Continuum elastic modeling of graphene resonators. *Nano Lett.*, 8(12):4196–4200, 2008.
- [70] D.-B. Zhang, E. Akatyeva, and T. Dumitrică. Bending ultrathin graphene at the margins of continuum mechanics. *Phys. Rev. Lett.*, 106:255503, Jun 2011.
- [71] Q. Lu, M. Arroyo, and R. Huang. Elastic bending modulus of monolayer graphene. *Journal of Physics D: Applied Physics*, 42:102002, 2009.
- [72] A. Fasolino, J. H. Los, and M. I. Katsnelson. Intrinsic ripples in graphene. *Nat Mater*, 6(11):858–861, 11 2007.
- [73] K. V. Zakharchenko, J. H. Los, M. I. Katsnelson, and A. Fasolino. Atomistic simulations of structural and thermodynamic properties of bilayer graphene. *Phys. Rev. B*, 81:235439, Jun 2010.
- [74] C. Lee, X. Wei, J. W. Kysar, and J. Hone. Measurement of the elastic properties and intrinsic strength of monolayer graphene. *Science*, 321(5887):385–388, 2008.
- [75] R. Nicklow, N. Wakabayashi, and H. G. Smith. Lattice dynamics of pyrolytic graphite. *Phys. Rev. B*, 5:4951–4962, Jun 1972.
- [76] M. Poot and H. S. J. van der Zant. Nanomechanical properties of few-layer graphene membranes. *Applied Physics Letters*, 92(6):063111–063111–3, feb 2008. ISSN 0003-6951. doi: 10.1063/1.2857472.
- [77] A.V. Pogorelov. *Bending of surfaces and stability of shells*, volume 72. American Mathematical Society, 1 edition, 1988.
- [78] B. Lassagne, Y. Tarakanov, J. Kinaret, D. Garcia-Sanchez, and A. Bachtold. Coupling mechanics to charge transport in carbon nanotube mechanical resonators. *Science*, 325(5944):1107–1110, 2009.
- [79] G. A. Steele, A. K. Hüttel, B. Witkamp, M. Poot, H. B. Meerwaldt, L. P. Kouwenhoven, and H. S. J. van der Zant. Strong coupling between single-electron tunneling and nanomechanical motion. *Science*, 325(5944):1103–1107, 2009.
- [80] M. Brink. *Imaging Single-Electron charging in nanostructures by low-temperature scanning force microscopy*. PhD thesis, Cornell University, 2007.

